

1                                   **Spectral Intensity Bioaerosol Sensor (SIBS):**  
2                                   **An Instrument for Spectrally Resolved Fluorescence Detection**  
3                                   **of Single Particles in Real-Time**

4  
5                   Tobias Könemann<sup>1</sup>, Nicole Savage<sup>2a</sup>, Thomas Klimach<sup>1</sup>, David Walter<sup>1</sup>, Janine Fröhlich-  
6                   Nowoisky<sup>1</sup>, Hang Su<sup>1</sup>, Ulrich Pöschl<sup>1</sup>, J. Alex Huffman<sup>2</sup>, and Christopher Pöhlker<sup>1</sup>

7  
8                   <sup>1</sup>*Max Planck Institute for Chemistry, Multiphase Chemistry Department, P.O. Box 3060, D-55020*  
9                   *Mainz, Germany*

10                  <sup>2</sup>*University of Denver, Department of Chemistry and Biochemistry, 2190 E. Iliff Ave., Denver, Col-*  
11                  *orado 80208, USA*

12  
13                  <sup>a</sup> *Now at Aerosol Devices Inc., 430 North College Avenue # 430, Fort Collins, Colorado 80524,*  
14                  *USA*

15  
16  
17  
18                  *Correspondence to: J. A. Huffman (alex.huffman@du.edu) and C. Pöhlker (c.pohlker@mpic.de)*

19  
20  
21  
22  
23  
24  
25  
26  
27                  Keywords: WIBS, bioaerosols, fluorescence spectroscopy, performance evaluation and characteriza-  
28                  tion, polystyrene latex spheres, biofluorophores, size and fluorescence calibration

## 29 **Abstract**

30 Primary biological aerosol particles (PBAP) in the atmosphere are highly relevant for the Earth sys-  
31 tem, climate, and public health. The analysis of PBAP, however, remains challenging due to their  
32 high diversity and large spatiotemporal variability. For real-time PBAP analysis, light-induced fluo-  
33 rescence (LIF) instruments have been developed and widely used in laboratory and ambient studies.  
34 The interpretation of fluorescence data from these instruments, however, is often limited by a lack of  
35 spectroscopic information. This study introduces an instrument – the Spectral Intensity Bioaerosol  
36 Sensor (SIBS, Droplet Measurement Technologies (DMT, Longmont, CO, USA)) – that resolves  
37 fluorescence spectra for single particles and, thus, promises to expand the scope of fluorescent PBAP  
38 quantification and classification.

39  
40 The SIBS shares key design components with the latest versions of the Wideband Integrated Bioaer-  
41 osol Sensor (WIBS) and the findings presented here are also relevant for the widely deployed WIBS-  
42 4A and WIBS-NEO as well as other LIF instruments. The key features of the SIBS and findings of  
43 this study can be summarized as follows:

- 44 - Particle sizing yields reproducible linear responses for particles in the range of 300 nm to 20  $\mu\text{m}$ .  
45 The lower sizing limit is significantly smaller than for earlier commercial LIF instruments (e.g.,  
46 WIBS-4A and the Ultraviolet Aerodynamic Particle Sizer (UV-APS)), expanding the analytical  
47 scope into the accumulation mode size range.
- 48 - Fluorescence spectra are recorded for two excitation wavelengths ( $\lambda_{\text{ex}} = 285$  and 370 nm) and a  
49 wide range of emission wavelengths ( $\lambda_{\text{mean}} = 302 - 721$  nm) with a resolution of 16 detection  
50 channels, which is higher than for most other commercially available LIF bioaerosol sensors.
- 51 - Fluorescence spectra obtained for 16 reference compounds confirm that the SIBS provides suffi-  
52 cient spectral resolution to distinguish major modes of molecular fluorescence. For example, the  
53 SIBS resolves the spectral difference between bacteriochlorophyll and chlorophyll *a/b*.
- 54 - A spectral correction of the instrument-specific detector response is essential to use the full fluo-  
55 rescence emission range.
- 56 - Asymmetry factor (AF) data were assessed and were found to provide only limited analytical  
57 information.
- 58 - In test measurements with ambient air, the SIBS worked reliably and yielded characteristically  
59 different spectra for single particles in the coarse mode with an overall fluorescent particle frac-  
60 tion of  $\sim 4\%$  ( $3\sigma$  threshold), which is consistent with earlier studies in comparable environments.

## 61 1. Introduction

62 Aerosol particles are omnipresent in the atmosphere, where they are involved in many environmental  
63 and biogeochemical processes (e.g., Baron & Willeke, 2001; Després et al., 2012; Fuzzi et al., 2006;  
64 Hinds, 1999; Pöschl, 2005; Pöschl & Shiraiwa, 2015). Primary biological aerosol particles (PBAP),  
65 also termed bioaerosols, represent a diverse group of airborne particles, consisting of whole or frag-  
66 mented organisms including, e.g., bacteria, viruses, archaea, algae, and reproductive units (pollen  
67 and fungal spores), as well as decaying biomass (e.g., Deepak & Vali, 1991; Després et al., 2012;  
68 Fröhlich-Nowoisky et al., 2016; Jaenicke, 2005; Madelin, 1994; Pöschl, 2005) and can span sizes  
69 from few nanometers up to  $\sim 100 \mu\text{m}$  (Hinds, 1999; Schmauss and Wigand, 1929). The increasing  
70 awareness of the importance of PBAP regarding aerosol-cloud interactions, health aspects, and  
71 spread of organisms on local, continental or even intercontinental scales has led to a growing interest  
72 by scientific researchers and the public (e.g., Després et al., 2012; Fröhlich-Nowoisky et al., 2016;  
73 Yao, 2018).

74 Due to inherent limitations (e.g., poor time resolution and costly laboratory analyses) of tradi-  
75 tional off-line techniques (e.g., light microscopy and cultivation-based methods) for PBAP quantifi-  
76 cation, several types of real-time techniques have been developed within the last several decades to  
77 provide higher time resolution and lower user costs (e.g., Caruana, 2011; Després et al., 2012;  
78 Fennelly et al., 2017; Ho, 2002; Huffman and Santarpia, 2017; Jonsson and Tjärnhage, 2014; Sodeau  
79 and O'Connor, 2016). One promising category of real-time instruments – meaning that particles are  
80 sampled and analyzed both instantly and autonomously – involves application of light- induced flu-  
81 orescence (LIF). The main principle of this technique is the detection of intrinsic fluorescence from  
82 fluorophores ubiquitous in biological cells, such as those airborne within PBAP. These fluorophores  
83 include a long list of biological molecules such as aromatic amino acids (e.g., tryptophan and tyro-  
84 sine), co-enzymes (e.g., reduced pyridine nucleotides (NAD(P)H)), flavin compounds (e.g., ribofla-  
85 vin), as well as biopolymers (e.g., cellulose and chitin) and chlorophyll (e.g., Hill et al., 2009; Li et  
86 al., 1991; Pan et al., 2010; Pöhlker et al., 2012, 2013). Detailed information of biological fluorophores  
87 can be found elsewhere (Pöhlker et al., 2012 and references therein).

88 Today, commercial on-line LIF instruments such as the Ultraviolet Aerodynamic Particle Sizer  
89 (UV-APS, TSI Inc. Shoreview, MN, USA) and the Wideband Integrated Bioaerosol Sensor (WIBS,  
90 developed by the University of Hertfordshire, U.K. and currently licensed and manufactured by  
91 Droplet Measurement Technologies (DMT, Longmont, CO, USA)) are commonly applied for re-  
92 search purposes. Detailed descriptions of the UV-APS (e.g., Agranovski et al., 2003; Brosseau et al.,  
93 2000; Hairston et al., 1997) and the WIBS series (e.g., Foot et al., 2008; Kaye et al., 2000, 2005;  
94 Stanley et al., 2011) are given elsewhere. Concisely, the UV-APS uses an  $\lambda_{\text{ex}} = 355 \text{ nm}$  laser excita-  
95 tion source and spans an emission range between  $\lambda_{\text{em}} = 420\text{-}575 \text{ nm}$ . In contrast, the WIBS applies

96 two pulsed xenon flash lamps emitting at  $\lambda_{\text{ex}}=280$  and 370 nm, whereas fluorescence emission is  
97 detected in three detection channels,  $\lambda_{\text{em}}=310-400$  nm (at  $\lambda_{\text{ex}}=280$  nm) and  $\lambda_{\text{em}}=420-650$  nm (at  
98  $\lambda_{\text{ex}}=280$  and 370 nm). Both instruments provide spectrally unresolved fluorescence information. The  
99 latest WIBS model is currently the WIBS-NEO, whose design is based on a WIBS-4A but with an  
100 extended particle size detection range between  $\sim 500$  nm and  $30\ \mu\text{m}$  (nominal). Both UV-APS and  
101 WIBS models have been examined in a variety of laboratory validations (e.g., Agranovski et al.,  
102 2003, 2004; Brosseau et al., 2000; Healy et al., 2012; Hernandez et al., 2016; Kanaani et al., 2007;  
103 O'Connor et al., 2013; Saari et al., 2013, 2014; Savage et al., 2017; Toprak & Schnaiter, 2013) and  
104 have been deployed to investigate both indoor and outdoor atmospheric aerosol via longer-term  
105 measurements (e.g., Bhangar et al., 2014; Calvo et al., 2018; Crawford et al., 2016; Fernández-  
106 Rodríguez et al., 2018; Foot et al., 2008; Gabey et al., 2010, 2013; Gosselin et al., 2016; Healy et al.,  
107 2014; Huffman et al., 2010, 2012, 2013; Ma et al., 2019; Perring et al., 2015; Schumacher et al.,  
108 2013; Twohy et al., 2016; Ziemba et al., 2016).

109 Although LIF instruments do not offer the same qualitative ability to identify sampled particles  
110 as, e.g., off-line microscopy, mass spectrometry, or culture-based methods, they provide size-re-  
111 solved information as well as fast sampling and fine-scale temporal information for single particles  
112 not accessible with off-line techniques. Nevertheless, these instruments present significant chal-  
113 lenges. For example, quantification of PBAP by LIF instruments is hindered by the fact that some  
114 biological materials reveal weak fluorescence characteristics that does not rise above detection  
115 thresholds (Huffman et al., 2012). In addition to this complication, the detection threshold is not a  
116 universally defined parameter and varies for each channel between different units of the same type  
117 of instruments (e.g., Hernandez et al., 2016; Savage et al., 2017). Furthermore, unambiguous spec-  
118 troscopic characterization of bioparticles is fundamentally challenging, because fluorescence spectra  
119 of even individual molecules in condensed matter are relatively broad due to radiative decay path-  
120 ways of excited electrons. Further, bioparticles are chemically complex, each comprised of a mixture  
121 of at least dozens of types of fluorophores that can each emit a unique emission spectrum that smears  
122 together into an even broader fluorescence spectrum from each particle (Hill et al., 2009, 2015; Pan,  
123 2015). Another difficulty is that many non-biological particles, such as certain mineral dusts and  
124 polycyclic aromatic hydrocarbons (PAHs), may fluoresce, making it more difficult to distinguish  
125 patterns arising from biological particles (e.g., Pöhlker et al., 2012 and references therein; Savage et  
126 al., 2017). Lastly, most currently available commercial LIF instrumentation are limited to recording  
127 data in 1-3 spectrally integrated emission channels, which limits the interpretation of fluorescence  
128 information. Recent efforts to apply more complex clustering algorithms to the spectrally unresolved  
129 WIBS-type data are proving helpful at adding additional discrimination (e.g., Crawford et al., 2015;  
130 Robinson et al., 2013; Ruske et al., 2017; Savage & Huffman, 2018). For example, it was shown for

131 a rural forest study in Colorado that a cluster derived using WIBS-3 data, assigned to fungal spores  
132 (Crawford et al., 2015), correlated well with the mass concentration of molecular fungal tracers (e.g.,  
133 arabitol and mannitol) measured with offline chemical techniques (Gosselin et al., 2016). In contrast,  
134 the clusters in the same study that were assigned to bacteria correlated only poorly with endotoxins,  
135 used as bacterial molecular tracers (Gosselin et al., 2016). This provides evidence of a limitation to  
136 using LIF instrumentation with low spectral resolution to separate or identify some PBAP types.  
137 Additionally, the bacterial cluster allocation might have also been hampered in that case by the min-  
138 imum detectable particle size of the WIBS ( $\sim 0.8 \mu\text{m}$ ), resulting in a lower detection efficiency for  
139 bacteria.

140 The evolution of LIF techniques over the last several decades has significantly expanded our  
141 knowledge on spatiotemporal patterns of PBAP abundance in the atmosphere. Nevertheless to further  
142 improve the applicability of LIF instrumentation to widespread PBAP detection, it is necessary both  
143 to design LIF instrumentation with adequate instrumental properties (e.g., high spectral resolution)  
144 and to standardize their operation by characterizing instruments thoroughly with known standards  
145 (Robinson et al., 2017). Working toward this goal, a number of LIF instruments have been developed  
146 to analyze single bioparticles by collecting resolved fluorescence spectra (e.g., Hill et al., 1999; Pan  
147 et al., 2010, 2003; Pinnick et al., 2004; Ruske et al., 2017), however relatively little has been done to  
148 offer these commercially. Examples for commercially available instruments providing resolved flu-  
149 orescence spectra are the PA-300 ( $\lambda_{\text{ex}} = 337 \text{ nm}$ ;  $\lambda_{\text{em}} = 390 - 600 \text{ nm}$ , 32 fluorescence detection chan-  
150 nels) (Crouzy et al., 2016; Kiselev et al., 2011, 2013) and the follow-up model Rapid-E ( $\lambda_{\text{ex}} = 337$   
151  $\text{nm}$ ;  $\lambda_{\text{em}} = 350 - 800 \text{ nm}$ , 32 fluorescence detection channels) (<http://www.plair.ch/>), both manufac-  
152 tured by Plair SA, Geneva, Switzerland. In addition to collecting resolved fluorescence spectra, both  
153 instruments also provide measurements of the decay of fluorescence signals, also referred to as flu-  
154 orescence lifetime.

155 Introduced here is an instrument for the detection and characterization of individual particles; the  
156 Spectral Intensity Bioaerosol Sensor (SIBS, Droplet Measurement Technologies). Technical proper-  
157 ties of the instrument are described in detail and its performance is validated with sizing and fluo-  
158 rescence particle standards, as well as with particles in ambient air. Due to the dual excitation and spec-  
159 trally resolved fluorescence in combination with a broad size detection range, the SIBS has the po-  
160 tential to increase the selectivity of fluorescent biological and non-biological particle detection and  
161 discrimination. Because the SIBS uses a comparable optical system as the WIBS-4A and WIBS-  
162 NEO, technical details presented here are broadly important to a growing community of scientists  
163 investigating both indoor and outdoor aerosol. Insights and data presented will thus contribute to  
164 ongoing discussions within the community of LIF users and will also stimulate discussions about  
165 needs for future instrument improvements.

## 166 2. Materials and methods

### 167 2.1 Chemicals and materials

168 Supplemental table S1 summarizes 19 polystyrene latex spheres (PSLs, 5 doped with fluorescent  
169 dye) and 6 polystyrene divinylbenzene (PS-DVB) particles, which were purchased from Thermo  
170 Fisher (Waltham, MA, USA), Bangs Laboratories Inc. (Fishers, IN, USA), Duke Scientific Corp.  
171 (Palo Alto, CA, USA), and Polysciences Inc. (Warrington, PA, USA). A detailed study regarding  
172 steady-state fluorescence properties of PSLs and PS-DVB particles used within this study can be  
173 found in Könemann et al. (2018). Additionally, we analyzed particles comprised separately of seven  
174 pure biofluorophores (tyrosine, tryptophan, NAD, riboflavin, chlorophyll *a* and *b*, and bacteriochloro-  
175 rophyll) (Table S2) as well as one microorganism (*Saccharomyces cerevisiae*; baker's yeast, bought  
176 at a local supermarket). Table S2 also includes reference particles used for asymmetry measurements,  
177 namely iron oxide (Fe<sub>3</sub>O<sub>4</sub>), carbon nanotubes, and ammonium sulfate. Ultrapure water (MilliQ, 18  
178 MΩ) and ≥ 99.8 % ethanol (CAS Nr. 64-17-5, Carl Roth GmbH und Co. KG, Karlsruhe, Germany)  
179 were used as solvents.

180

### 181 2.2 Aerosolization of reference particles

182 PSLs were aerosolized from aqueous suspensions with a portable aerosol generator (AG-100; DMT).  
183 For both fluorescent and non-fluorescent PSLs, one drop of the suspension (or alternatively three  
184 drops for 3 and 4 μm PSLs) was diluted into 10 ml ultrapure water in plastic medical nebulizers  
185 (Allied Healthcare, St. Louis, MO, USA). The majority of water vapor from the aerosolization pro-  
186 cess condenses inside the mixing chamber (~570 cm<sup>3</sup>) of the aerosol generator. By using a tempera-  
187 ture and relative humidity (RH) sensor (MSR 145 data logger, MSR Electronics GmbH, Seuzach,  
188 Switzerland) monitoring the flow directly after the aerosol generator we measured RH values of  
189 ~33% (sample flow: 1.4 l/min, dilution: 5 l/min), ~39% (sample flow: 1.4 l/min, dilution: 4 l/min),  
190 and ~54% (sample flow: 2.3 l/min, dilution: 2 l/min). Because of the low RH measured, we did not  
191 use additional drying (e.g., diffusion dryer) to decrease humidity in the sample flow. Hence, the outlet  
192 of the aerosol generator was directly connected to the SIBS inlet with ~30 cm of conductive tubing  
193 (1/4 inch). PSLs were measured for 1 min. Non-fluorescent 4.52 μm PSLs were measured for 2 min,  
194 because of the low number concentrations due to poor aerosolization efficiency and gravitational  
195 settling of larger particle sizes.

196 *S. cerevisiae* was analyzed using a method similar to the one stated above, with the exceptions  
197 that the suspension was prepared with a spatula tip of material mixed into ultrapure water and that a  
198 diffusion dryer (20 cm, 200 g silica) was added to remove excess water vapor. *S. cerevisiae* was

199 measured for 5 min. Chlorophyll *a*, *b*, and bacteriochlorophyll samples were diluted in 10 ml ethanol.  
200 Between each measurement, the setup was cleaned by aerosolizing ultrapure water for 5 min.

201 PS-DVB particles and biofluorophores (Table S1 and S2) were aerosolized in a dry state. For this  
202 purpose, air at a flowrate of  $\sim 0.6$  l/min was sent through a HEPA filter into a 10 ml glass vial. A  
203 small amount of each solid powder sample ( $\sim 1$  g) was placed inside the vial and entrained into the  
204 particle-free airstream. Additionally, the sample was physically agitated by tapping the vial. The  
205 outlet was connected with  $\sim 20$  cm conductive tubing into the inlet of the SIBS. The tubing and glass  
206 vial were cleaned after each measurement to prevent particle contaminations from previous measure-  
207 ments. Each powder was sampled until cumulative number concentrations  $> 5000$  particles were  
208 reached.

209 In contrast to the monodisperse and spherical PSL standards, the biofluorophore aerosolization  
210 process provided a polydisperse and morphologically heterogeneous particle distribution with sig-  
211 nificant particle fractions at sizes  $< 1$   $\mu\text{m}$ . Therefore, we only used particles in a size range between  
212 1 and 2  $\mu\text{m}$  with sufficient fluorescence intensity values for subsequent data analysis. The only ex-  
213 ceptions are the chlorophyll types, where a size range between 0.5 and 2  $\mu\text{m}$  (chlorophyll *a* and *b*)  
214 and 0.5 and 1  $\mu\text{m}$  (bacteriochlorophyll) were used due to a less efficient particle aerosolization.

215 The fluorescent background of the SIBS was measured daily by firing the xenon lamps into the  
216 optical chamber in the absence of particles (forced trigger mode). In this case, the diaphragm pump  
217 was turned off and the inlet blocked to prevent particles reaching the optical chamber. One forced  
218 trigger mode was performed per day with 100 xenon shots per min over a duration of 5 min. The  
219 average background signal ( $+ 1\sigma$  standard deviation (SD)) was subtracted from derived fluorescence  
220 emission of each sample. Additionally, the background signal was reviewed periodically between  
221 each biofluorophore measurement to verify that, e.g., optical components were not coated with resi-  
222 dues from previous measurements. No significant changes in background signal were observed be-  
223 tween individual measurements. Optimization of the thresholding strategy is still an on-going work,  
224 for example to investigate whether the often applied  $3\sigma$  threshold used for the WIBS (e.g., Gabey et  
225 al., 2010) also works well with respect to the optical setup of the SIBS. For the assessment of the  
226 accuracy of measured fluorescence emissions from reference compounds, a threshold of  $1\sigma$  was used  
227 here.

228 For particle asymmetry measurements, iron (II, III) oxide ( $\text{Fe}_3\text{O}_4$ ), carbon nanotubes, and ammo-  
229 nium sulfate were aerosolized in dry state, and 2  $\mu\text{m}$  non-fluorescent PSLs and ultrapure water were  
230 aerosolized with the aerosol generator method outlined above with SIBS integration times of 3 min  
231 in all cases. Due to the broad distribution of asymmetry factor (AF) values for particles below 1  $\mu\text{m}$ ,  
232 only the size fraction  $\geq 1$   $\mu\text{m}$  was used for subsequent analyses. Furthermore, we observed that AF  
233 bins between 0 and 1, and AF bin 100 tend to produce increased signal responses, especially for high

234 particle concentrations, for which they were discarded within the analyses. The origin of this effect  
235 is unknown. However, one explanation could be optical coincidences caused by high particle con-  
236 centrations, resulting in multiple particles being simultaneously present within the scattering volume,  
237 as reported by Cooper (1988) using forward-scattering signatures of cloud probes.

238 For collection of particles for microscopy measurements, the sample flow was bypassed and led  
239 through a custom-made particle impactor, which was connected to a mass flow controller (D-6321-  
240 DR, Bronkhorst High-Tech B.V., Ruurlo, Netherlands) and a membrane pump (N816.1.2KN.18,  
241 KNF, Freiburg, Germany). Particles were collected out of the sample flow onto glass cover slips (15  
242 mm diameter) at a flow rate of 2 l/min over a duration of 1 min.

243

### 244 **2.3 Reference fluorescence spectra**

245 A Dual-FL fluorescence spectrometer (Horiba Instruments Incorporated, Kyoto, Japan) was used as  
246 an offline reference instrument to validate the SIBS spectra. Aqualog V3.6 (Horiba) software was  
247 used for data acquisition. The spectrometer was manufacturer-calibrated with NIST Fluorescence  
248 Standard Reference Materials (SRMs 2940, 2941, 2942, and 2943). Aforementioned standard fluor-  
249 ophores were analyzed using the SIBS excitation wavelengths at  $\lambda_{\text{ex}} = 285$  and 370 nm. The Dual-  
250 FL<sup>1</sup> spectrometer uses a xenon arc lamp as excitation source and a CCD (charge-coupled device) as  
251 emission detector, capable of detecting fluorescence emission between 250 and 800 nm. Unless oth-  
252 erwise stated, a low detector gain setting (2.25 e<sup>-</sup> per count) and an emission resolution of 0.58 nm  
253 was used for all measurements with the Dual-FL. Subsequently, we use the term “reference spectra”  
254 for all measurements performed with the Dual-FL. In total, 100 individual spectra were recorded for  
255 each sample and averaged spectra were analyzed in Igor Pro (Wavemetrics, Lake Oswego, Oregon  
256 USA). Background measurements (solvent in the absence of particles) were taken under the same  
257 conditions as for sample measurements and subtracted from the emission signal. For direct compar-  
258 ison to spectra recorded by the SIBS, reference spectra were re-binned by taking the sum of the  
259 fluorescence intensity within the spectral bin width of each SIBS detection channel (Table 1).

260 For PSL measurements, 1.5  $\mu\text{l}$  of each PSL stock solution was diluted in 3.5 ml ultrapure water  
261 in a 10 x 10 x 40 mm UV quartz cuvette (Hellma Analytics, Müllheim, Germany) and constantly  
262 stirred with a magnetic stirrer to avoid particle sedimentation during measurements. Chlorophyll *a*  
263 and *b* and bacteriochlorophyll were handled equally, however concentrations were individually ad-  
264 justed to prevent the detector from being saturated and to avoid self-quenching or inner filter effects  
265 (Sinski and Exner, 2007). Concentrations were used as follows: chlorophyll *a*: 300 nmol/l, chloro-  
266 phyll *b*: 1  $\mu\text{mol/l}$ , and bacteriochlorophyll: 3  $\mu\text{mol/l}$ . PSLs, chlorophyll *b*, and bacteriochlorophyll

---

<sup>1</sup> Technical information taken from Dual-FL operation manual, rev. A, 30 NOV 2012; Horiba.



267 measurements were performed with an integration time of 2 s. For chlorophyll *a* an integration time  
268 of 1 s was used.

269 All other biofluorophores, *S. cerevisiae*, and PS-DVB particles were measured in dry state using  
270 a front surface accessory (Horiba). The sample was placed into the surface holder and covered with  
271 a synthetic fused silica window. To limit detector saturation from more highly fluorescent particle  
272 types, the surface holder was placed at a 70° angle to the fluorescence detector for NAD and ribofla-  
273 vin, 75° for tyrosine, 80° for *S. cerevisiae*, and 85° for tryptophan and PS-DVB particles and subse-  
274 quently excited at  $\lambda_{\text{ex}}=285$  and 370 nm. Emission resolution and detector gain settings were used as  
275 for measurements of samples in solution, except for an integration time of 1 s for all dry samples.  
276 Background measurements were performed as described above and subtracted from each sample.  
277 Excitation-emission matrices (EEMs) were measured with the same samples as for single wavelength  
278 measurements. EEMs were recorded at excitation wavelengths between  $\lambda_{\text{ex}} = 240$  and 800 nm (1 nm  
279 increments) and an emission range between  $\lambda_{\text{em}} = 247$  and 829 nm (0.58 nm increments). Exposure  
280 times of 1 s were used, except for 2  $\mu\text{m}$  green, 3  $\mu\text{m}$  non-fluorescent PSLs (2 s), and NAD (0.5 s).  
281 EEMs were analyzed using Igor Pro.

282

#### 283 **2.4 Calibration lamps and spectral correction**

284 The relative responsivity of a fluorescence detector can vary substantially across its emission range  
285 and, therefore, must be spectrally corrected as a function of emission wavelength (e.g., DeRose, 2007;  
286 Lakowicz, 2004). For spectral correction it was important to choose: (i) light sources covering the  
287 full spectral emission range of the SIBS, with temporal stability on the timescale of many months  
288 and (ii) a calibrated and independent spectrometer to serve as spectral reference.

289 A deuterium-halogen lamp (DH-Mini; Ocean Optics, Largo, FL, USA) and a halogen projector  
290 lamp (EHJ 24 V, 250 W; Ushio Inc., Tokyo, Japan) were used as calibration light sources. Both  
291 lamps were connected to a 50 cm optical fiber (FT030, Thorlabs, Newton, NJ, USA) and vertically  
292 fixed inside the optical chamber of the Dual-FL spectrometer. An aluminum mirror was attached to  
293 the end fitting of the optical fiber, reflecting light in a 90° angle into the detector opening. The pro-  
294 jector halogen lamp was allowed to warm up for 30 s before each measurement. For all power levels  
295 (100, 150, 200, and 250 W), an integration time of 3 s was used. The DH-Mini was operational for  
296 30 min before each measurement. Settings were used as for the projector halogen lamp, however,  
297 due to the low emission a high detector gain setting (9 e<sup>-</sup> per count) was used with an integration time  
298 of 25 s. As described in Sect. 2.3, 100 single measurements were taken and averaged (Fig. S1). For  
299 the SIBS, both light sources were measured in the same way as for the reference spectra. Measure-

300 ments were performed with a detector amplification at 610 V (see Sect. 4.2). Background measure-  
301 ments were taken as described in Sect. 2.2. Projector halogen lamp spectra (at all power levels) were  
302 recorded for 3 min, the DH-Mini, due to its low emission intensity, for a duration of 5 min.

303 For the halogen projector lamp, averaged intensity values in each spectral bin were acquired at  
304 each power level (150, 200, and 250 W). Spectra measured at 100 W were discarded due to the low  
305 and unstable emission at wavelengths shorter than  $\sim 500$  nm (Fig. S1). Reference spectra and spectra  
306 recorded by the SIBS were normalized onto the SIBS detection channel 9 ( $\lambda_{\text{mean}} = 528.0$  nm), which  
307 is, theoretically, the detection channel with the highest responsivity (see Sect. 4.3). The individual  
308 spectral correction factors were calculated by dividing the reference spectra by the spectra derived  
309 from the SIBS. The final correction factors are a combination of both light sources where the detec-  
310 tion channels 1-5 ( $\lambda_{\text{mean}} = 302.2 - 415.6$  nm) include the correction factors for the DH-Mini and the  
311 detection channels 6-16 ( $\lambda_{\text{mean}} = 443.8 - 721.1$  nm) the correction factors for the halogen projector  
312 lamp. At the intersection between channel 5 and 6, both corrections (DH-Mini, halogen) are in good  
313 agreement ( $\Delta_{\text{correction}} = 0.6$  in channel 6). For all particle measurements described in the following  
314 sections, the background signal and raw sample spectra recorded by the SIBS were multiplied by  
315 those correction factors.

316

## 317 **2.5 Microscopy of selected reference particles**

318 Bright field microscopy was conducted using an Eclipse Ti2 (Nikon, Tokyo, Japan) with a 60x im-  
319 mersion oil objective lens and an additional optical zoom factor of 1.5, resulting in a 90x magnifica-  
320 tion. Glass cover slips, used as collection substrates in the particle impactor (Sect. 2.2), were put onto  
321 a specimen holder and fixed with tape. Images were recorded using a DS Qi2 monochrome micro-  
322 scope camera with 16.25 megapixels and z-stacks of related images were created using the software  
323 NIS-Elements AR (both Nikon).

324

## 325 **2.6 Ambient measurement setup and data analysis**

326 The SIBS was operated between the 5<sup>th</sup> of April to the 7<sup>th</sup> of May 2018 from a fourth floor roof  
327 laboratory at the Max Planck Institute for Chemistry in Mainz, Germany (49°59'28.2"N,  
328 8°13'44.5"E) similar to measurements as described in Huffman et al. (2010) using a UV-APS. The  
329 period between the 12<sup>th</sup> and 18<sup>th</sup> of April 2018 is described here to highlight the capability of the  
330 SIBS to monitor ambient aerosol. Beside of the SIBS, four additional instruments (data not shown  
331 within this study) were connected with  $\sim 20$  cm conductive tubing ( $1/4$  inch) to a sample airflow  
332 splitter (Grimm Aerosol Technik GmbH & Co. KG, Ainring, Germany). The splitter was connected  
333 to 1.5 m conductive tubing ( $5/8$  inch), bent out of the window, and connected to 2.4 m stainless steel

334 tubing ( $\frac{5}{8}$  inch, Dockweiler AG, Neustadt-Glewe, Germany) vertically installed. Between a TSP  
335 head (total suspended particles, custom-made) and the stainless steel tubing, a diffusion dryer (1 m,  
336 1 kg silica) was installed. Silica was exchanged every third to fourth day and periodic forced trigger  
337 measurements were performed daily. The total flow was  $\sim 8.4$  l/min.

338 For measurements presented here, particles were only included if they showed fluorescence emis-  
339 sion in at least two consecutive spectral channels. This filter was applied to limit noise introduced  
340 from measurement artifacts from a variety of sources and will need to be investigated in more detail.  
341 The conservative analysis approach here suggests that the values reported are likely to be a lower  
342 limit for fluorescent particle number and fraction. The observations are in line with previous meas-  
343 urements, however, giving general support that the SIBS measurements are reasonable. Note that the  
344 maximum repetition rate of the xenon lamps is 125 Hz, corresponding to maximum concentrations  
345 of 20 particles per  $\text{cm}^{-3}$  (see Sect. 3.3). Because  $\sim 50\%$  of the total coarse particle number were excited  
346 by xenon 1 and xenon 2, the fluorescent particle concentrations and fluorescent fractions are cor-  
347 rected accordingly.

348

### 349 **3. Design and components of the SIBS**

350 The SIBS is based on the general optical design of the WIBS-4A (e.g., Foot et al., 2008; Healy et al.,  
351 2012; Hernandez et al., 2016; Kaye et al., 2005; Perring et al., 2015; Robinson et al., 2017; Savage  
352 et al., 2017; Stanley et al., 2011) with improvements based on a lower particle sizing limit, resolved  
353 fluorescence detection, and a broader emission range. The instrument provides information about  
354 size, particle asymmetry, and fluorescence properties for individual particles in real-time. The exci-  
355 tation wavelengths are optimized for the detection of the biological fluorophores tryptophan,  
356 NAD(P)H, and riboflavin. However, other fluorophores in PBAP will certainly fluoresce at these  
357 excitation wavelengths as many of them cluster in two spectral fluorescence “hotspots” as summa-  
358 rized in Pöhlker et al. (2012 and references therein) and as shown for WIBS-4A measurements by  
359 Savage et al. (2017). Figure 1 shows an overview of excitation wavelengths and emission ranges of  
360 the UV-APS, WIBS-4A, WIBS-NEO, and SIBS for bioaerosol detection in relation to the spectral  
361 location of selected biofluorophores, such as tyrosine, tryptophan, NAD(P)H, riboflavin, and chloro-  
362 phyll *b*. At  $\lambda_{\text{ex}} = 285$  nm, the SIBS excites fluorophores in the “protein hotspot”, at  $\lambda_{\text{ex}} = 370$  nm  
363 fluorophores in the “flavin/coenzyme hotspot” (Pöhlker et al., 2012). In contrast to the UV-APS, the  
364 SIBS is able to detect fluorescence signals from chlorophyll due to the extended upper spectral range  
365 of detection (up to  $\lambda_{\text{em}} = 721$  nm). Both the WIBS-4A and WIBS-NEO cover the spectral emission  
366 range for chlorophyll *b*, however, cannot provide resolved spectral information to separate it from  
367 other fluorophores. Table 2 summarizes and compares parameters and technical components of the

368 SIBS, WIBS-4A, and WIBS-NEO. The individual components are described in detail in the subse-  
369 quent sections.

370 To avoid potential misunderstanding, it is important to note that the SIBS described in this study  
371 is not related to spark-induced breakdown spectroscopy instrumentation, which uses the same acro-  
372 nym (e.g., Bauer & Sonnenfroh, 2009; Hunter et al., 2000; Khalaji et al., 2012; Schmidt & Bauer,  
373 2010). The DMT SIBS discussed here was recently used as part of a study investigating aerosols in  
374 several ambient outdoor environments (Nasir et al., 2018), but the study here is the first to discuss  
375 important technical details of the instrument design and operation.

376

### 377 **3.1 Aerosol inlet and flow diagram**

378 The design for the aerosol inlet of the SIBS is identical to the inlet of the WIBS-4A and WIBS-NEO.  
379 A detailed flow diagram is shown in Figure 2a. Aerosol is drawn in via an internal pump as laminar  
380 air flow through a tapered delivery nozzle (Fig. 2a(1)) where sheath (~2.2 l/min) and sample flow  
381 (~0.3 l/min) are separated.

382

### 383 **3.2 Size and shape analysis**

384 After passing the delivery nozzle, entrained particles traverse a 55 mW continuous-wave diode laser  
385 at  $\lambda = 785$  nm (position #1 in Fig. 2b and #2 in Fig. S2). Unlike in the WIBS-4A and WIBS-NEO  
386 (635 nm diode laser), the triggering laser in the SIBS is in the near-infrared (IR) region ( $> 700$  nm)  
387 and, therefore, outside the detectable emission range of the 16-channel photomultiplier tube (PMT)  
388 to avoid scattered light from the particle trigger laser being detected (see Fig. 1). The side and forward  
389 scattered light is collected and used for subsequent measurements. Side scattered light is collected  
390 by two concave mirrors, which are directed at  $90^\circ$  from the laser beam axis, and reflect the collected  
391 light onto a dichroic beam splitter (#7 in Fig. S2). A PMT (H10720-20, Hamamatsu Photonics K.K.,  
392 Japan) converts incoming light signals into electrical pulses, which are used for particle triggering  
393 and sizing (#6 in Fig. S2). For the determination of the optical particle size, the SIBS uses a calculated  
394 calibration curve according to the Lorenz-Mie Theory, assuming spherical and monodisperse PSLs  
395 with a refractive index of 1.59 (Brandrup et al., 1989; Lorenz, 1890; Mie, 1908). Compared to aero-  
396 dynamic sizing, which depends on particle morphology and density (e.g., Reid et al., 2003; Reponen  
397 et al., 2001), the calculated optical diameter can vary significantly if the assumption of sphericity is  
398 not fulfilled. In contrast, optical sizing is not as affected by differences in material density. The in-  
399 strument operator must thus be aware of uncertainties in measured particle size due to, e.g., particle  
400 morphology, spatial orientation of a particle when traversing the trigger laser or changing refractive  
401 indices. In contrast to the WIBS-4A, the SIBS and WIBS-NEO detect the full range of particle sizes

402 (SIBS: ~0.3 and 100  $\mu\text{m}$  (nominal); WIBS-NEO: ~0.5 and 30  $\mu\text{m}$  (nominal)) by using one PMT gain  
403 setting instead of switching between a “Low Gain” and “High Gain” setting. Physical and technical  
404 details of this Gain-switching method are patent pending and are not publicly available.

405 The forward-scattered light is measured by a quadrant PMT (#5 in Fig. S2) to detect the scatter  
406 asymmetry for each particle (Kaye et al., 1991, 1996). A OG-515 long pass filter (Schott AG, Mainz,  
407 Germany) prevents incoming light from the xenon flash lamps in a spectral range below  $515 \pm 6$  nm  
408 from reaching the Quadrant PMT. To calculate the AF, the root-mean-square variations for each  
409 quadrant of the PMT of the forward-scattered light intensities are used (Gabey et al., 2010). The AF  
410 broadly relates whether a particle is more spherical or fibril. Theoretically, for a perfectly spherical  
411 particle, the AF would be 0, whereas an elongated particle would correspond to an AF of 100 (Kaye  
412 et al., 1991). However, due to electrical and optical noise of the Quadrant PMT, the AF value of a  
413 sphere is usually between ca. 2 and 6 (according to WIBS-4A service manual (DOC-0345 Rev A)).  
414 Because the AF value depends on physical properties of optical components, the baseline for spher-  
415 ical particles may shift even within identical instruments (Savage et al., 2017). For example, the study  
416 by Toprak & Schnaiter (2013) reported an average AF value for spherical particles of 8 using a  
417 WIBS-4A. In contrast, AF values shown by Foot et al. (2008) were, on average, below ~5 for  
418 spherical particles measured with a WIBS-2s prototype.

419

### 420 **3.3 Fluorescence excitation**

421 Two xenon flash lamps (L9455-41, Hamamatsu) (#3 and #4 in Fig. S2) are used to induce fluores-  
422 cence. They emit light pulses, which exhibit a broad excitation wavelength range of 185 to 2000 nm.  
423 The light is optically filtered to obtain a relatively monochromatic excitation wavelength. Further  
424 information about spectral properties of the xenon flash lamps can be found elsewhere (Specification  
425 sheet TLSZ1006E04, Hamamatsu, May 2015). Figure 3 displays relevant optical properties of the  
426 lamps and filters used within the SIBS, WIBS-4A, and WIBS-NEO. For the SIBS, a BrightLine®  
427 FF01-285/14-25 (Semrock Inc., Rochester, NY, USA) single-band bandpass filter is used with  $\lambda_{\text{mean}}$   
428 = 285 nm and an effective excitation band<sup>2</sup> of 14 nm width is used for xenon 1. For xenon 2, the  
429 single-band bandpass filter BrightLine® FF01-370/36-25 (Semrock) is used with  $\lambda_{\text{mean}} = 370$  nm and  
430 with an effective excitation band of 36 nm width. The only difference between all three instruments  
431 is that the WIBS-4A and WIBS-NEO use a different single-band bandpass filter for xenon 1 (Sem-  
432 rock, BrightLine® FF01-280/20-25;  $\lambda_{\text{mean}} = 280$  nm; effective excitation band of 20 nm). The exci-  
433 tation light beam for all three instruments is focused on the sample flow within the optical cavity,

---

<sup>2</sup> The effective excitation band is defined as “guaranteed minimum bandwidth” (GMBW), describing the spectral region a bandpass filter transmits light relative from the mean wavelength. For example, a GMBW of 14 nm means that light is transmitted in a 7 nm spectral range above and below the mean wavelength.

434 resulting in a rectangular beam shape of ~5 mm by 2 mm. Xenon 1 is triggered when particles pass  
435 position 2 in Figure 2b and approximately 10  $\mu$ s later xenon 2 is triggered as the particles move  
436 further to position 3 in Figure 2b. After firing, the flash lamps need ~5 ms to recharge. During the  
437 recharge period, particles are counted and sized but no fluorescence information is recorded. The  
438 maximum repetition rate of the xenon lamps yields a measurable particle number concentration of  
439  $\sim 2 \times 10^4 \text{ l}^{-1}$  (corresponding to  $20 \text{ cm}^{-3}$ ).

440 Irradiance values from light sources becomes a crucial factor when interpreting derived fluores-  
441 cence data of LIF instruments because the fluorescence intensity is directly proportional to the inten-  
442 sity of incident radiant power, described by the relationship:

$$443 \quad F = \phi I_0(1 - e^{-\epsilon bc}) \quad (1)$$

444  $\phi$ : quantum efficiency,  $I_0$ : intensity of incident light,  $\epsilon$ : molar absorptivity,  $b$ : path length (cell),  $c$ :  
445 molar concentration (Guilbault, 1990).

446 To measure the irradiance of each xenon lamp after optical filtering, we used a thermal power  
447 head (S425C, Thorlabs), which was placed at a distance of 11.3 cm (focus length from xenon arc  
448 bow to sample flow intersection) from the xenon lamp measuring over a duration of 1 min at 10  
449 xenon shots per s. By measuring new xenon lamps, we observed an average irradiance of 14.8  
450  $\text{mW}/\text{cm}^2$  for xenon 1 and 9.6  $\text{mW}/\text{cm}^2$  for xenon 2, corresponding to ~154 % higher irradiance (spec-  
451 trally integrated) from xenon 1. A second set of lamps, used intermittently for three years including  
452 several months of continuous ambient measurements and a lab study with high particle concentra-  
453 tions, exhibited average irradiance values of 10.8  $\text{mW}/\text{cm}^2$  ( $1\sigma$  SD 1.8  $\text{mW}/\text{cm}^2$ ) for xenon 1 and 4.9  
454  $\text{mW}/\text{cm}^2$  ( $1\sigma$  SD 1.9  $\text{mW}/\text{cm}^2$ ) for xenon 2, corresponding to ~220 % higher irradiance from xenon  
455 1. Comparing the nominal, transmission-corrected irradiance data from the two xenon lamps pro-  
456 vided by the lamp supplier (Fig. 3a and 3b, red dashed lines), an irradiance imbalance between xenon  
457 1 and xenon 2 can be assumed for all three LIF instruments discussed here (SIBS, WIBS-4A, and  
458 WIBS-NEO).

459 Results shown here are comparable to multiple WIBS studies (e.g., Hernandez et al., 2016;  
460 Perring et al., 2015; Savage et al., 2017), where fluorescence emission intensities at  $\lambda_{\text{ex}} = 280 \text{ nm}$   
461 (xenon 1) also show a tendency to be higher than those at  $\lambda_{\text{ex}} = 370 \text{ nm}$  (xenon 2).

### 462 3.4 Spectrally resolved fluorescence detection

463 Fluorescence emission from excited particles is collected by two parabolic mirrors in the optical  
464 cavity and delivered onto a custom-made dichroic beam splitter (Semrock, #7 in Fig. S2). The beam

468 splitter allows transmission of incoming light between ~300 and 710 nm, with an average transmis-  
469 sion efficiency of 96%. At wavelengths shorter than 300 nm, the transmission decreases rapidly to <  
470 20% at 275 nm. At the upper detection end of the SIBS ( $\lambda_{\text{mean}} = 721$  nm), the transmission efficiency  
471 decreases to ~89%. The scattering light from the diode laser is reflected at a 90° angle onto the PMT  
472 used for particle detection and sizing. At the excitation wavelength of 785 nm, the reflection effi-  
473 ciency is stated at ~95% (Fig. S3).

474 After passing the dichroic beamsplitter, the photons are led into a grating polychromator (A  
475 10766, Hamamatsu) (#8 in Fig. S2). A custom-made transmission grating (Hamamatsu) is used to  
476 diffract incoming light within a nominal spectral range between 290.8 – 732.0 nm. In case of the  
477 SIBS, a grating with 300 g/mm groove density and 400 nm blaze wavelength is used, resulting in a  
478 nominal spectral width of 441.2 nm and a resolution of 28.03 nm/mm. After passing the transmission  
479 grating, the diffracted light hits a 16-channel linear array multi-anode PMT (H12310-40, Hamama-  
480 tsu) (#9 in Fig. S2) with defined mean wavelengths for each channel as shown in Table 1.

481 For each single particle detected, two spectra are recorded, at  $\lambda_{\text{ex}} = 285$  and 370 nm. The detect-  
482 able band range of the PMT overlaps the excitation wavelength of xenon 2. Therefore, a notch optical  
483 filter (Semrock) is placed between the optical chamber and the grating polychromator to prevent the  
484 detector from being saturated. Incoming light at wavelengths shorter than 300 nm and from 362 to  
485 377 nm is blocked from reaching the PMT resulting in a reduced spectral bin width for detection  
486 channels 1, 3 and 4. The first three detection channels are omitted because their mean wavelengths  
487 are below  $\lambda_{\text{ex}} = 370$  nm (see also Fig. 1). Accordingly, the emission spectra for xenon 2 excitation  
488 begin at channel 4 ( $\lambda_{\text{mean}} = 387.3$  nm).

489 Technical data (xenon flash lamps, filters, dichroic beam splitter, PMT responsivity, and trans-  
490 mission grating) described in the previous sections (3.3 and 3.4) were provided by Hamamatsu and  
491 Semrock. Note that transmission/reflection efficiencies of the dichroic beam splitter, cathode radiant  
492 sensitivity of the PMT, and diffraction efficiency data are modeled. Thus, individual components  
493 may differ slightly from modeled values, even within the same production batch. Neither company  
494 assumes data accuracy or provides warranty, either expressed or implied.

495 The SIBS was originally designed and marketed to record time- and spectrally-resolved fluores-  
496 cence lifetimes at two excitation wavelengths. The fluorescence lifetime of most biofluorophores,  
497 serving as targets for bioaerosol detection, are usually below 10 ns (e.g., Chorvat & Chorvatova,  
498 2009; Herbrich, et al., 2012; O'Connor et al., 2014; Richards-Kortum & Sevick-Muraca, 1996).  
499 However, by choosing xenon lamps as excitation source, recording relevant fluorescence lifetimes  
500 in this ns range is hampered by the relatively long decay time of the xenon lamp excitation pulse  
501 (~1.5  $\mu$ s). In principle, fluorescence lifetime measurements would be possible if the xenon lamps  
502 were replaced by appropriate laser excitation sources in the SIBS optical design.

### 503 **3.5 Software components and data output**

504 The SIBS uses an internal computer (#10 in Fig. S2) with embedded LabView-based data acquisition  
505 software allowing the user to control functions in real time and change multiple measurement param-  
506 eters. As an example, the “Single Particle” tab out of the SIBS interface is shown in Figure S4. Here,  
507 the user can define, e.g., the sizing limits of the SIBS (upper and lower threshold) and the minimum  
508 size of a particle being excited by the xenon flash lamps. Furthermore, forced trigger measurements  
509 can be performed while on this particular tab. Subsequently, the term “forced trigger measurement”  
510 will be replaced by “background signal measurement”. A local Wi-Fi network is installed so that the  
511 SIBS can be monitored and controlled remotely. A removable hard drive is used for data storage.  
512 Data is stored in a HDF5 format to minimize storage space and optimize data write speed. Resulting  
513 raw data are processed in Igor Pro. As an example: by using a minimum sizing threshold of 500 nm,  
514 the SIBS data output per day, operating in a relatively clean environment ( $\sim 40$  particles per  $\text{cm}^{-3}$ ),  
515 can span several hundreds of MB. In contrast, the data output can increase up to  $\sim 3$  GB daily in  
516 polluted areas ( $\sim 680$  particles per  $\text{cm}^{-3}$ ). By lowering the minimum sizing threshold to 300 nm, the  
517 data volume can exceed 10 GB per day when sampling in a moderately polluted environment ( $\sim 180$   
518 particles per  $\text{cm}^{-3}$ ).

519

## 520 **4. Results and data validation**

### 521 **4.1 Validation of SIBS sizing**

522 To validate the optical sizing of the SIBS, twenty particle size standards were analyzed, covering a  
523 broad size range from 0.3 to 20  $\mu\text{m}$  in particle diameter. Overall, the particle size measurements from  
524 the SIBS (optical diameter) show good agreement with the corresponding measurements of physical  
525 diameter reported by PSL and PS-DVB manufacturers (Fig. 4). For the SIBS, the manufacturer states  
526 a nominal minimum size detection threshold of 300 nm. Figure 4 shows that a linear response be-  
527 tween optical particle size and physical particle size extends down to at least 300 nm. Smaller parti-  
528 cles were not investigated. The upper size detection threshold is reported by the manufacturer to be  
529 nominally 100  $\mu\text{m}$ . However, the upper limit was not investigated here due to the difficulty in aero-  
530 solizing particles larger than this. In most field applications, the upper particle size cut is often far  
531 below this value due to unavoidable sedimentation losses of large particles in the inlet system (e.g.,  
532 Moran-Zuloaga et al., 2018.; Von der Weiden et al., 2009). Note that the size distributions of physical  
533 diameter for PS-DVB standards are broader compared to the PSL standards, as reported by the man-  
534 ufacturer (Table S1). This also translates to broader distributions of optical diameter measured by the  
535 SIBS for PS-DVB than for PSL particles. The 0.356  $\mu\text{m}$  PSL sample was an outlier with respect to  
536 the overall trend, showing an optical diameter of 0.54  $\mu\text{m}$ . We suspect that this deviation between



537 physical and optical size can be explained by a poor quality of this particular PSL sample lot rather  
538 than an instrumental issue, and so it was not included in the calculation of the trend line (Fig. 4).  
539 Furthermore, the SIBS was shown to slightly undersize the PSLs between 0.6 and 0.8  $\mu\text{m}$ , however,  
540 the overall trend exhibits a coefficient of determination of  $r^2 > 0.998$ .

541 As mentioned in Sect. 3.2, an important point regarding the SIBS and WIBS-NEO is that the size  
542 calibration within the unit cannot be changed by the user, meaning that the PMT output voltages are  
543 transformed directly to outputted physical diameter within the internal computer using a proprietary  
544 calculation. It is still important, however, for the user to perform sizing calibration checks frequently  
545 to verify and potentially post-correct particle sizing of all particle sizing instruments, including the  
546 SIBS and WIBS-NEO.

547

## 548 **4.2 Amplification of fluorescence detector**

549 As with all optical detection techniques, adequate understanding of detection thresholds is an essen-  
550 tial aspect of instrument characterization and use (e.g., Jeys et al., 2007; Savage et al., 2017). Appli-  
551 cation of appropriate voltage gain settings must be applied to the physical detection process so as not  
552 to lose information about particles that cannot be recovered by post-processing of data. Yet particles  
553 in the natural atmosphere exhibit an extremely broad range of fluorescence intensities (many orders  
554 of magnitude), arising from the breadth of quantum yields for fluorophores occurring in aerosols and  
555 from the steep increase of fluorescence emission intensity with particle size ( $2^{\text{nd}}$  to  $3^{\text{rd}}$  power) (e.g.,  
556 Hill et al., 2015; Könemann et al., 2018; Sivaprakasam et al., 2011; Swanson & Huffman, 2018).  
557 This range of fluorescence properties is generally broader than the dynamic range of any single in-  
558 strument, and so a UV-LIF instrument can be operated, e.g., to either: (i) apply a higher detector gain  
559 to allow high sensitivity toward detecting weakly fluorescing particles, often from rather small par-  
560 ticles ( $< 1 \mu\text{m}$ ), at the risk of losing fluorescence information for large or strongly fluorescent parti-  
561 cles due to detector saturation or (ii) apply a lower detector gain to preferentially detect a wide range  
562 of more highly fluorescent particles, but at the risk of not detecting weakly fluorescent or small par-  
563 ticles.

564 Amplification voltage of the 16-channel PMT used in the SIBS can be adjusted between 500 and  
565 1200 V. Each of the 16 detection channels can also be individually adjusted using digital gain settings  
566 within the SIBS acquisition software. This channel-specific gain does not affect the amplification  
567 process (e.g., the dynode cascade), but rather modifies the output signal of single detection channels  
568 digitally. The digital gain is applied only after the signal collection process, and so cannot compensate  
569 for a signal that is below the noise threshold or that saturates the detector. The digital gain was thus  
570 left at the maximum gain level (255 arbitrary units (a.u.)) for all channels during particle measure-  
571 ments discussed here.

572 To explore the influence of amplification voltage on particle detectability, 0.53  $\mu\text{m}$  purple PSLs  
573 were chosen to arbitrarily represent the lower limit of detectable fluorescence intensity. Using larger  
574 (0.96  $\mu\text{m}$ ) particles comprised of the same purple fluorophore, Könemann et al. (2018) showed that  
575 the particles were only narrowly detectable above the fluorescence threshold in each of the three  
576 channels of a WIBS-4A (same unit as used in Savage et al., 2017) and so the smaller, 0.53  $\mu\text{m}$  PSLs  
577 were chosen here as a first proxy for the most weakly fluorescing particles we would expect to detect.  
578 To improve the signal to noise ratio (SNR) for the lower fluorescence detection limit, the PMT am-  
579 plification voltage was varied in seven steps between 500 and 1000 V (corresponding to a gain from  
580  $10^3$  to  $10^6$ , specification sheet TPMO1060E02, Hamamatsu, June 2016) for purple PSLs and back-  
581 ground signals (Fig. 5a). Whereas PSL spectra at a PMT amplification of 500 V were indistinguish-  
582 able from the background signal ( $+ 1\sigma$  SD), spectra show a discernable peak at  $\lambda_{\text{mean}} = 415.6$  nm  
583 above 600 V. Subsequently, the SIBS was operated with a PMT amplification voltage of 610 V  
584 corresponding to the lowest SNR threshold accepted (Fig. 5a, b). The detection of small biological  
585 particles was tested by measuring the emission spectrum of *S. cerevisiae* as an example of a PBAP  
586 (see also Pöhlker et al., 2012). On average, the size of intact *S. cerevisiae* particles range between  $\sim 2$   
587  $- 10$   $\mu\text{m}$  (e.g., Pelling et al., 2004; Shaw et al., 1997). To test the ability of the SIBS to detect low  
588 intensity emissions, we separately analyzed *S. cerevisiae* particles between 0.5 and 1  $\mu\text{m}$ , which most  
589 likely includes cell fragments caused by the aerosolization process (Fig. 5c). The tryptophan-like  
590 emission, peaking in detection channel 2 ( $\lambda_{\text{mean}} = 330.6$  nm) for  $\lambda_{\text{ex}} = 285$  nm, reveals intensity values  
591 below 100 a.u., which are comparable to fluorescence intensity values derived from 0.53  $\mu\text{m}$  purple  
592 PSLs (detection channel 5,  $\lambda_{\text{mean}} = 415.6$  nm, Fig. 5d). These two tests for *S. cerevisiae* and 0.53  $\mu\text{m}$   
593 purple PSLs confirmed the instruments ability to detect emission spectra from particles at least as  
594 strongly fluorescent as these two test cases, leaving a wide range to detect larger and more intensely  
595 fluorescing particles. By using a  $3\sigma$  SD threshold, the fluorescence peak at  $\lambda_{\text{mean}} = 415.6$  nm of 0.53  
596  $\mu\text{m}$  purple PSLs is still detectable but cannot be distinguished from the background signal at a  $6\sigma$  SD  
597 threshold anymore. Therefore, fluorescence intensity values at the lower detection limit should be  
598 treated with care. Corrected spectra of both *S. cerevisiae* and 0.53  $\mu\text{m}$  purple PSLs can be found in  
599 the supplement (Fig. S5). By operating the SIBS at relatively low detector amplification, very weak  
600 fluorescence, especially from small particles ( $< 1$   $\mu\text{m}$ ) might not exceed the detection threshold dur-  
601 ing field applications and would be missed. Further investigation will be necessary to choose ampli-  
602 fication voltages appropriate for individual applications where smaller or otherwise weakly fluores-  
603 cent particles might be particularly important. For all subsequent measurements discussed here, a  
604 PMT amplification voltage of 610 V was used.

605 Saturation only occurred for 15 and 20  $\mu\text{m}$  non-fluorescent PS-DVB particles. As highlighted in  
606 Figure S6, the polystyrene/detergent signal (Könemann et al., 2018) at  $\lambda_{\text{ex}} = 285$  nm for 10  $\mu\text{m}$  PS-

607 DVB particles can be spectrally resolved (Fig. S6b), whereas the spectrum for 15  $\mu\text{m}$  PS-DVB par-  
608 ticles (Fig. S6e) is altered due to single particles ( $\sim 10\%$  out of 400 particles) saturating the detector  
609 (at 62383 a.u.). By comparing the defined lower detection end (Fig. 5) to the upper end (Fig. S6), a  
610 quantitative difference of approximately three orders of magnitude can be estimated, indicating a  
611 wide detectable range at the chosen amplification voltage setting.

612

### 613 **4.3 Wavelength-dependent spectral correction of detector**

614 The 16 cathodes of the PMT should be considered as independent detectors with wavelength depend-  
615 ent, individual responsivity and amplification characteristics. In combination with physical properties  
616 of technical components (e.g., excitation sources, optical filters, gratings), an instrumental-specific  
617 spectral bias might result in incorrect or misleading spectral patterns if not corrected (e.g., DeRose,  
618 2007; DeRose et al., 2007; Holbrook et al., 2006). To compensate for such potential instrumental  
619 biases, we used a spectral correction approach as described in Sect. 2.4. The spectral correction fac-  
620 tors are comparable to the theoretical responsivity of the PMT with the highest correction for chan-  
621 nels 1-4 ( $\lambda_{\text{mean}} = 302.2 - 387.3\text{ nm}$ ) and 14-16 ( $\lambda_{\text{mean}} = 666.5 - 721.1\text{ nm}$ ) (Fig. 6). Channel 8 ( $\lambda_{\text{mean}} =$   
622  $500.0\text{ nm}$ ) shows the highest responsivity and channels 6 and 7 ( $\lambda_{\text{mean}} = 443.8$  and  $471.9\text{ nm}$ ) exhibit  
623 a noticeable lower responsivity than their adjacent channels (see also Sect. 4.4.1). The spectral cor-  
624 rection shows several peaks (e.g., detector channels 3, 5, and 8) and dips (e.g., detector channels 4,  
625 6, and 7) (Fig. 6), however, this pattern is due to gain variations for different channels and is not  
626 noise.

627 It is important to note that the detector settings and spectral correction uniquely refer to the SIBS  
628 unit as it was used for the current study. Due to technical and physical variability as stated above, it  
629 is likely that the spectral correction required for other SIBS units would be somewhat different. Fur-  
630 thermore, the wavelength-dependent detector correction may change over time due to material fa-  
631 tigue or contaminations in the optical chamber affecting background signal measurements. Periodic  
632 surveillance and adjustments are therefore required, especially after measurements where the instru-  
633 ment was exposed to high particle concentrations or was operated during extreme weather or envi-  
634 ronmental conditions (e.g., temperature, humidity, vibration). For particle sizing verification, we rec-  
635 ommend the use of 0.5, 1, and 3  $\mu\text{m}$  non-fluorescent PSLs. Regarding a fluorescence response check,  
636 we recommend 2  $\mu\text{m}$  green and 2  $\mu\text{m}$  red PSLs for the validation of the spectral responsivity maxi-  
637 mum and the upper (near-IR) detection range. To our knowledge, no fluorescent dyed PSLs are avail-  
638 able to verify the response within the lower spectral detection range (UV) of the SIBS. However, the  
639 polystyrene signal of 3  $\mu\text{m}$  non-fluorescent PSLs (Fig S6g, h, i, see also Könemann et al., 2018)  
640 represents a compromise between signal strength at  $\lambda_{\text{ex}} = 285\text{ nm}$  and aerosolization efficiency (com-  
641 pared to PSLs with larger sizes) for a spectral responsivity validation.

## 642 4.4 Fluorescence spectra of standards

### 643 4.4.1 PSL standards

644 The SIBS spectra for the four different PSL standards, covering an emission range from UV to near-  
645 IR, generally agree well with the corresponding reference spectra (Fig. 7). Each of the two excitation  
646 wavelengths probe separate fluorescent modes, which appear at approximately the same emission  
647 wavelength for a given PSL type (e.g.,  $\lambda_{em} = \sim 580$  nm for red PSLs, Fig. 7j), as discussed by  
648 Könemann et al. (2018). Moreover, even the rather weak polystyrene and detergent fluorescence,  
649 systematically associated with PSL suspensions (Könemann et al., 2018), is resolved by the SIBS at  
650  $\lambda_{ex} = 285$  nm and  $\lambda_{em} = \sim 300$  nm (Fig. 7b, e, h, k). It is further noteworthy that emission intensity at  
651  $\lambda_{ex} = 285$  nm is generally higher than derived emission intensity at  $\lambda_{ex} = 370$  nm (Fig. 7c, f, i, l),  
652 supporting the finding that a particle receives higher irradiance values from xenon 1 than from xenon  
653 2 (see also Sect. 3.3).

654 As mentioned in Sect. 4.3, detection channels 6 and 7 require relatively large correction factors.  
655 For 2.07  $\mu\text{m}$  purple PSLs (Fig. 7b, c), the SIBS spectra closely match the references spectra after  
656 correction. For the 2.1  $\mu\text{m}$  blue PSLs (Fig. 7e, f), however, the corrected spectrum matches the ref-  
657 erence spectrum well, except at detection channel 6 ( $\lambda_{mean} = 443.8$  nm), where the SIBS spectrum is  
658 lower than the reference spectrum by approximately 50%. This effect was also observed for 1  $\mu\text{m}$   
659 blue PSLs (Thermo Fisher, B0100), doped with the same fluorophore (data not shown). The reason  
660 for this discrepancy is unknown. Nevertheless, because this effect only occurs noticeably for highly  
661 fluorescent blue PSLs and NAD (see also Sect. 4.4.2), one explanation could be that the instrument-  
662 dependent dynode cascade (the electronic amplification stages) for this particular detection channel  
663 is suppressed, resulting in a lower amplification efficiency. In this case, relatively low signals could  
664 be amplified correctly, whereas medium or high intensity emission could only be amplified up to a  
665 certain level. The amplification threshold for detection channel 6 is, however, unknown and needs  
666 further verification.

667

### 668 4.4.2 Biofluorophore standards

669 Figure 8 and 9 highlight fluorescence spectra of different biofluorophores measured by the SIBS,  
670 which correspond to related reference spectra (compare also Pöhlker et al., 2012), showing that amino  
671 acids (fluorescence emission only at  $\lambda_{ex} = 285$  nm), co-enzymes and flavin compounds (fluorescence  
672 emission at  $\lambda_{ex} = 285$  and 370 nm), and chlorophylls (fluorescence emission only at  $\lambda_{ex} = 370$  nm)  
673 can be spectrally distinguished.

674 The uncorrected spectrum of tryptophan (Fig. S8) highlights the necessity of a spectral correction  
675 to compensate for the low detector responsivity within the UV and near-IR bins. If the fluorescence

676 signal of tryptophan remains uncorrected, the spectra is shifted slightly to longer wavelengths (red-  
677 shifted) due to the low responsivity of channel 2 in comparison to channel 3, resulting in misleading  
678 spectral information. For NAD (Fig. 8h, i), fluorescence intensity values of channel 6 are lowered  
679 due the suppressed amplification efficiency in this particular channel as described for blue PSLs  
680 (Sect. 4.4.1).

681 All biofluorophores (except chlorophyll types) were aerosolized as dry powders (see Sect. 2.2)  
682 to avoid fluorescence solvatochromism effects (e.g., Johnson et al., 1985). Solvatochromism of fluor-  
683 ophores in aqueous solution – the only atmospherically relevant case – typically shifts fluorescence  
684 emissions to longer wavelengths due to the stabilized excited state caused by polar solvents  
685 (Lakowicz, 2004). This spectral red-shift can be seen in Figure S9, where the peak maximum for  
686 NAD shows a difference of ~15 nm between a dry and water-solvated state, whereas riboflavin re-  
687 veals an even higher shift of ~37 nm. Here, solvatochromism serves as an example for fluorescence  
688 spectra that vary substantially as a function of the fluorophore’s microenvironments (e.g., solvent  
689 polarity, pH, temperature).

690 Each of the three types of chlorophyll exhibit the weakest emission of all biofluorophores meas-  
691 ured within this study, however the SIBS was able to detect the fluorescence signal at  $\lambda_{\text{ex}} = 370$  nm  
692 for all three (Fig. 9). The spectral difference between chlorophyll *a* and *b* is only minor at  $\lambda_{\text{ex}} = 370$   
693 nm ( $\Delta\lambda = 8.3$  nm) for which the spectral resolution of the SIBS is not capable of distinguishing be-  
694 tween types (Fig. 9a, b, c, d and Fig. S10) (e.g., French et al., 1956; Welschmeyer, 1994). Neverthe-  
695 less, the SIBS shows the ability to distinguish between chlorophyll *a* and *b*, and bacteriochlorophyll  
696 due to the red-shift in the bacteriochlorophyll spectrum ( $\Delta\lambda = 28.5$  nm at  $\lambda_{\text{ex}} = 370$  nm, between  
697 chlorophyll *a* and bacteriochlorophyll). This may provide a further discrimination level regarding  
698 algae, plant residues, and cyanobacteria. Bacteriochlorophyll also shows a second and even stronger  
699 emission peak at  $\lambda_{\text{ex}} = 370$  nm ( $\lambda_{\text{em}} = \sim 800$  nm) that could help further distinguish it from chlorophyll  
700 *a* and *b*, but the SIBS spectrometer cannot currently detect this far into the IR (e.g., Rijgersberg et  
701 al., 1980; Van Grondelle et al., 1983).

702 Overall, fluorescence emissions recorded by the SIBS are in good agreement with measured ref-  
703 erence spectra. However, care must be taken as to the interpretation of fluorescence emissions cov-  
704 ering broad spectral ranges, which span regimes with large differences between individual correction  
705 factors (e.g., channel 15 ( $\lambda_{\text{mean}} = 693.9$  nm, Fig.7l) and channel 2 ( $\lambda_{\text{mean}} = 330.6$  nm, Fig.8k). For the  
706 SIBS, namely the first two UV detection channels and the last two near-IR channels should be treated  
707 with care. Further investigation is required for a careful assessment of how the spectral correction  
708 can be applied properly with respect to fluorescent and non-fluorescent atmospheric particles.

709  
710

## 711 **4.5 Particle asymmetry measurements**

712 The AF of spherical particles such as PSLs (Fig. 10a, b) and ultrapure water droplets is approximately  
713 10 (Table 3), which is slightly higher than reported values for spherical particles by, e.g., Savage et  
714 al. (2017) (AF= ~5) or Toprak & Schnaiter (2013) (AF= ~8) using a WIBS. It is noteworthy that the  
715 AF of water droplets increases slightly with increasing droplet size and, therefore, contributes to the  
716 mean value (Fig. S12). This effect is most likely based on a decreasing surface tension with increas-  
717 ing droplet size for which the droplet morphology is changed to a more oval shape within the sample  
718 flow. A similar effect regarding a potential droplet deformation using an Airborne Particle Classifier  
719 (APC) was observed by Kaye et al., (1991). Even if the morphology of ammonium sulfate (crystal-  
720 line, Fig. 10d) and Fe<sub>3</sub>O<sub>4</sub> (irregular clusters, Fig. 10f) is diverse, the difference in AF is only minor  
721 (~13 and 14, Table 3), indicating that most naturally occurring aerosols (e.g., sea salt, soot, various  
722 bacterial and fungal clusters) will occur in a AF regime between ~10 and 20. Only rod-shaped carbon  
723 nanotubes (110-170 nm diameter, 5-9 μm length) show increased AFs with a mean value at ~22  
724 (Table 3) at which also, e.g., bacteria would occur (Fig. 10h). No particles observed exhibited average  
725 AF values >25, as would have been expected for, e.g., carbon nanotubes. Because the range of AF  
726 values for homogenous particles is relatively broad and the differences between morphologically  
727 diverse particle types is only minor (Table 3), the question can be raised to what extent particles  
728 could be distinguished based on the AF under ambient conditions. Similar broad AF ranges were  
729 found in Healy et al., (2012), measuring sodium chloride, chalk, and several pollen and fungal spores  
730 types. As also discussed by Savage et al. (2017), the AF values reported by SIBS and WIBS units  
731 should be treated with extreme care.

732 The validation of asymmetry measurements is challenging due to unavoidable particle and aero-  
733 solization effects (e.g., particle agglomeration and spatial orientation within the sample flow) and the  
734 lack of standardized procedures for AF calibrations. Measurements performed in this study do, there-  
735 fore, only serve as a rough AF assignment. Moreover, even if both the SIBS and WIBS use the same  
736 technical components for defining AFs, a direct intercomparison cannot be applied due to technical  
737 variability (e.g., PMT related signal-to-noise ratio or the alignment of optical components). Addi-  
738 tionally, it is currently unknown in how far the 785 nm diode laser of the SIBS affect asymmetry  
739 measurements compared to the WIBS using a 635 nm diode laser.

740

## 741 **4.6 Initial ambient measurements**

742 Several weeks of initial ambient SIBS measurements were conducted on the roof of the Max Planck  
743 Institute for Chemistry in Mainz, Germany. At a nearby building site, Huffman et al. (2010) con-  
744 ducted one of the first ambient UV-APS studies in the year 2006. Moreover, Toprak & Schnaiter

745 (2013) conducted a WIBS-4A study at a comparable site in central Germany from 2010 to 2011. The  
746 aim of this brief ambient section is to validate that the SIBS-derived key aerosol and fluorescence  
747 data are reasonable and relatively consistent with the aforementioned studies. We found a good agree-  
748 ment between the coarse mode ( $\geq 1 \mu\text{m}$ ) number concentrations ( $N_{T,c}$ ) of the SIBS ( $N_{T,c}$  ranging from  
749  $0.25$  to  $1.59 \text{ cm}^{-3}$ , with a mean of  $0.76 \text{ cm}^{-3}$ ) and previous data from the UV-APS (mean  $N_{T,c}$ :  $1.05$   
750  $\text{ cm}^{-3}$  (Huffman et al., 2010)) and the WIBS-4A (mean  $N_{T,c}$ :  $0.58 \text{ cm}^{-3}$  (Toprak and Schnaiter, 2013))  
751 (Fig.11a). Furthermore, good agreement was found between coarse mode fluorescent number con-  
752 centrations ( $N_{F,c}$ ) of the SIBS (mean  $N_{F,c(3\sigma)}$ :  $0.025 \text{ cm}^{-3}$ ), the UV-APS (mean  $N_{F,c}$ :  $0.027 \text{ cm}^{-3}$   
753 (Huffman et al., 2010)), and the WIBS-4A (mean  $N_{F,c(3\sigma)}$ :  $0.031 \text{ cm}^{-3}$  (Toprak and Schnaiter, 2013))  
754 (Fig.11a). Similarly, the fraction of fluorescent particles in the coarse mode ( $N_{F,c}/N_{T,c}$ ) compares well  
755 between SIBS (mean  $N_{F,c(3\sigma)}/N_{T,c}$ :  $4.2 \%$ ), the UV-APS (mean  $N_{F,c}/N_{T,c}$ :  $3.9 \%$  (Huffman et al.,  
756 2010)), and the WIBS-4A (mean  $N_{F,c(3\sigma)}/N_{T,c}$ :  $7.3 \%$  (Toprak and Schnaiter, 2013)) (Fig.11b). Ex-  
757 pectedly, a  $1\sigma$  SD threshold gives much higher SIBS fluorescent fractions of  $39.2 \%$ , whereas a  $6\sigma$   
758 SD threshold corresponds with much lower fluorescent fractions of  $1\%$  (Fig.11b). Note that no pre-  
759 fect match between our results and the studies by Huffman et al. (2010), and Toprak & Schnaiter  
760 (2013) can be expected, since the measurements took place with different sampling setups and during  
761 different seasons. Furthermore, the spectrally resolved SIBS data makes the definition of fluorescent  
762 fraction more complex than for UV-APS and WIBS data (see Sect. 2.6). However, the overall good  
763 agreement confirms that the SIBS produces reasonable results in an ambient setting. Further, the  
764 single particle fluorescence spectra are reasonable with respect to typical biofluorophore emissions  
765 (Pöhlker et al., 2012). Exemplary spectra ( $\lambda_{\text{ex}} = 285$  and  $370 \text{ nm}$ ) of ambient single particles can be  
766 found in the supplement (Fig.S13). An in-depth analysis of extended SIBS ambient datasets is subject  
767 of ongoing work.

768

## 769 **5. Summary and conclusions**

770 Real-time analysis of atmospheric bioaerosols using commercial LIF instruments has largely been  
771 restricted to data recorded in only 1-3 spectrally integrated emission channels, limiting the interpre-  
772 tation of fluorescence information. Instruments that can record resolved fluorescence spectra over a  
773 broad range of emission wavelengths may thus be required to further improve the applicability of  
774 LIF instrumentation to ambient PBAP detection. Introduced here is the SIBS (DMT, Longmont, CO,  
775 USA), which is an instrument that provides resolved fluorescence spectra ( $\lambda_{\text{mean}} = 302 - 721 \text{ nm}$ )  
776 from each of two excitation wavelengths ( $\lambda_{\text{ex}} = 285$  and  $370 \text{ nm}$ ) for single particles. The current  
777 study introduces the SIBS by presenting and experimentally validating its key functionalities. This  
778 work critically assesses the strengths and limitations of the SIBS with respect to the growing interest

779 in real-time bioaerosol quantification and classification. It should be noted that the study is an inde-  
780 pendent evaluation that was not conducted, endorsed, or co-authored by the manufacturer or repre-  
781 sentatives. Overall, this work confirms a precise particle sizing between 300 nm and 20  $\mu\text{m}$  and the  
782 particle discrimination ability based on spectrally resolved fluorescence information of several stand-  
783 ard compounds.

784 The SIBS was operated at a low PMT detector amplification setting (610 V) to retain capacity to  
785 detect large or brightly fluorescent particles. It was confirmed, however, that even weak fluorescence  
786 signals from 0.53  $\mu\text{m}$  purple PSLs and from small *S. cerevisiae* fragments (0.5 - 1  $\mu\text{m}$ ) can be clearly  
787 distinguished from the background signal. Saturation events were only observed for the polysty-  
788 rene/detergent signal from relatively large 15 and 20  $\mu\text{m}$  PS-DVB particles. Nevertheless, the fluo-  
789 rescence intensity detection threshold is highly instrument-dependent due to the complex interaction  
790 of single technical components across individual instruments. For example, xenon 1 exhibited ~154  
791 % higher irradiance than xenon 2 (both new lamps) due to differences in the properties of xenon  
792 emission and the optical filters used. For used xenon lamps (> 4000 hours of use), an even higher  
793 difference of ~220 % was observed. Thus, a defined fluorescence detection threshold will most likely  
794 change over time due to, e.g., material fatigue. Additionally, variable irradiance properties might  
795 significantly contribute to observed differences in performance of similar instrument types (e.g.,  
796 Hernandez et al., 2016), expressly underlining the need for a fluorescence calibrant applicable across  
797 LIF-instruments (e.g., Robinson et al., 2017). Nevertheless, to the best of our knowledge, there is  
798 currently no standard reference available that fulfills the requirements to serve as a calibrant for  
799 multi-channel, multi-excitation LIF-instruments. Observations in this study are valid not only for the  
800 SIBS, but also for the WIBS-4A and WIBS-NEO and lead to important implications for interpretation  
801 of particle data. In particular, a particle that exhibits measurable fluorescence in WIBS channel FL1,  
802 but only weak fluorescence in channel FL3 could be assigned as an “A-type” particle in one instru-  
803 ment but an “AC-type” particle in an instrument with slightly stronger xenon 2 irradiance. These  
804 differences in classification can be extremely important to interpretation of ambient data (e.g., Perring  
805 et al., 2015; Savage et al., 2017).

806 The PMT used in the SIBS shows a wavelength-dependent sensitivity distribution along all 16  
807 detection channels. To compensate for this characteristic and to be able to use the broadest possible  
808 fluorescence emission range, the measured emission spectra were corrected with respect to reference  
809 spectra acquired from deuterium and halogen lamps. A spectral correction over a broad emission  
810 range also introduces drawbacks, however, that LIF-instrument users should keep in mind while in-  
811 terpreting derived fluorescence information. In particular, the first two (UV) and the last two (near-  
812 IR) detection channels should be treated with care, because they require larger correction factors  
813 compared to adjacent channels. Ultimately, the correction factor and amplification voltages applied



814 to the detector will be experiment-specific and will need to be investigated with respect to individual  
815 experimental aims. To this extent, possible differences between instruments and important calibra-  
816 tions complicate the concept of the instrument being commercially available. Individual users may  
817 desire to be able to purchase the SIBS as a “plug-and-play” detector, but using without a critical  
818 understanding of these complexities would not be appropriate at this time and could lead to inadvert-  
819 ent misinterpretation of the data.

820 Fluorescence spectra of fluorescent PSLs, amino acids, co-enzymes, and flavins measured by the  
821 SIBS agree well with corresponding spectra recorded with an offline reference spectrometer. Thus,  
822 the SIBS was shown to be capable of clearly distinguishing between different particle types based on  
823 resolved fluorescence information. Furthermore, the extended fluorescence emission range ( $\lambda_{em} = >$   
824 700 nm) enables the SIBS also to distinguish chlorophyll *a* and *b* from bacteriochlorophyll, poten-  
825 tially opening new possibilities for the detection of, e.g., algae, plant residues, and cyanobacteria.

826 Particle asymmetry measurements revealed that spherical PSLs have an AF of 9.9 ( $\pm$  3.6),  
827 whereas other materials (ammonium sulfate, Fe<sub>3</sub>O<sub>4</sub>, and carbon nanotubes) show AF values of 13.1  
828 ( $\pm$  8.1), 14.4 ( $\pm$  7.4), and 21.6 ( $\pm$  12.7), respectively. Because differences of measured AF value  
829 between morphologically diverse particle types are small and within the ranges of uncertainty for the  
830 measurement of a given set of particles, it is questionable how well particles can be distinguished  
831 based on the AF as presently measured by the quadrant PMT. Users of SIBS and WIBS instruments  
832 should apply extreme care if using AF data. It is also likely that different instrument units may have  
833 very different AF responses with respect to this measurement. At a minimum, each individual unit  
834 needs to be rigorously calibrated to known particle types to determine if AF values are sufficiently  
835 different (e.g., separated by several standard deviations) to justify scientific conclusions based on the  
836 metric.

837 Exemplary ambient data, measured between the 12<sup>th</sup> and 18<sup>th</sup> of April 2018 on the roof of the  
838 Max Planck Institute for Chemistry in Mainz (Germany), are consistent with LIF measurement data  
839 using a UV-APS (Huffman et al., 2010) and a WIBS-4A (Toprak and Schnaiter, 2013). Total coarse  
840 particle number concentrations revealed a mean value of 0.76 cm<sup>-3</sup> (1.05 cm<sup>-3</sup> (Huffman et al., 2010);  
841 0.58 cm<sup>-3</sup> (Toprak and Schnaiter, 2013)) of which ~4.2% are considered to be fluorescent using a 3 $\sigma$   
842 SD threshold (3.9% (Huffman et al., 2010); 7.3% (Toprak and Schnaiter, 2013)), including only par-  
843 ticles that show fluorescence emission in at least two adjoining detection channels. Using a 1 $\sigma$  and  
844 6 $\sigma$  SD threshold results in fluorescent fractions of 39.2% and 1% respectively. However, the applica-  
845 bility of different threshold strategies for the SIBS is currently under investigation and needs further  
846 verifications.

847 The results suggest that the SIBS has the ability to increase the selectivity of detection of fluo-  
848 rescent biological and non-biological particles by use of two excitation wavelengths and 16-channel

849 resolved fluorescence information in combination with a broad detectable emission range. The ap-  
850 plicability of described methods onto ambient datasets is currently under investigation. Data shown  
851 here and the detailed insights of technical components used in the SIBS will be broadly beneficial  
852 for users of LIF instruments providing resolved fluorescence information, but also for users of vari-  
853 ous generations of WIBS and other LIF instruments widely applied within the bioaerosol community.

854

## 855 **6. Data availability**

856 The data of the key results presented here can be provided upon request. For specific data requests,  
857 please refer to the corresponding authors.

858

## 859 **Acknowledgements**

860 This work was supported by the Max Planck Society (MPG) and the Max Planck Graduate Center  
861 with the Johannes Gutenberg-University Mainz (MPGC). Financial support for Nicole Savage was  
862 provided by the Phillipson Graduate Fellowship from the University of Denver. We thank Maria  
863 Praß, Mira Pöhlker, Jan-David Förster, Meinrat O. Andreae, Peter Hoor, Viviane Després, Benjamin  
864 Swanson, Jorge Saturno, Bruna Holanda, Florian Ditas, Daniel Moran-Zuloaga, Björn Nillius, Jing  
865 Ming, Gavin McMeeking, Gary Granger, Alexis Attwood, Greg Kok, Robert MacAllister, John  
866 Walker, Matt Mahin, Matt Freer, Uwe Kuhn, Minghui Zhang, Petya Yordanova, Naama Lang-Yona,  
867 and members of the Mainz Bioaerosol Laboratory (MBAL) for their support and stimulating discus-  
868 sions.

## 869 7. References

- 870 Agranovski, V., Ristovski, Z., Hargreaves, M., Blackall, P. . and Morawska, L.: Real-time measurement of bacterial  
871 aerosols with the UVAPS: performance evaluation, *J. Aerosol Sci.*, 34(3), 301–317, doi:10.1016/S0021-  
872 8502(02)00181-7, 2003.
- 873 Agranovski, V., Ristovski, Z. D., Ayoko, G. A. and Morawska, L.: Performance evaluation of the UVAPS in measuring  
874 biological aerosols: Fluorescence spectra from NAD(P)H coenzymes and riboflavin, *Aerosol Sci. Technol.*, 38(4),  
875 354–364, doi:10.1080/02786820490437505, 2004.
- 876 Baron, P. A. and Willeke, K.: *Aerosol fundamentals*, *Aerosol Meas. Princ. Tech. Appl.*, 2, 2001.
- 877 Bauer, A. J. R. and Sonnenfroh, D. M.: Spark-induced breakdown spectroscopy-based classification of bioaerosols, in  
878 Safety, Security & Rescue Robotics (SSRR), 2009 IEEE International Workshop on, pp. 1–4, IEEE., 2009.
- 879 Bhangar, S., Huffman, J. A. and Nazaroff, W. W.: Size-resolved fluorescent biological aerosol particle concentrations and  
880 occupant emissions in a university classroom, *Indoor Air*, 24(6), 604–617, <https://doi.org/10.1111/ina.12111>,  
881 2014.
- 882 Brandrup, J., Immergut, E. H., Grulke, E. A., Abe, A. and Bloch, D. R.: *Polymer handbook*, Wiley New York etc., 1989.
- 883 Brosseau, L. M., Vesley, D., Rice, N., Goodell, K., Nellis, M. and Hairston, P.: Differences in detected fluorescence among  
884 several bacterial species measured with a direct-reading particle sizer and fluorescence detector, *Aerosol Sci.*  
885 *Technol.*, 32(6), 545–558, <https://doi.org/10.1080/027868200303461>, 2000.
- 886 Calvo, A. I., Baumgardner, D., Castro, A., Fernández-González, D., Vega-Maray, A. M., Valencia-Barrera, R. M., Oduber,  
887 F., Blanco-Alegre, C. and Fraile, R.: Daily behavior of urban fluorescing aerosol particles in northwest Spain,  
888 *Atmos. Environ.*, 184, 262–277, <https://doi.org/10.1016/j.atmosenv.2018.04.027> 2018.
- 889 Caruana, D. J.: Detection and analysis of airborne particles of biological origin: present and future, *Analyst*, 136(22), 4641–  
890 4652, doi: 10.1039/C1AN15506G, 2011.
- 891 Chorvat, D. and Chorvatova, A.: Multi-wavelength fluorescence lifetime spectroscopy: a new approach to the study of  
892 endogenous fluorescence in living cells and tissues, *Laser Phys. Lett.*, 6(3), 175–193, doi:10.1002/lapl.200810132,  
893 2009.
- 894 Cooper, W. A.: Effects of coincidence on measurements with a forward scattering spectrometer probe, *J. Atmos. Ocean.*  
895 *Technol.*, 5(6), 823–832, [https://doi.org/10.1175/1520-0426\(1988\)005<0823:EOCOMW>2.0.CO;2](https://doi.org/10.1175/1520-0426(1988)005<0823:EOCOMW>2.0.CO;2), 1988.
- 896 Crawford, I., Ruske, S., Topping, D. O. and Gallagher, M. W.: Evaluation of hierarchical agglomerative cluster analysis  
897 methods for discrimination of primary biological aerosol, *Atmos. Meas. Tech.*, 8(11), 4979–4991,  
898 <https://doi.org/10.5194/amt-8-4979-2015>, 2015.
- 899 Crawford, I., Lloyd, G., Bower, K. N., Connolly, P. J., Flynn, M. J., Kaye, P. H., Choularton, T. W. and Gallagher, M. W.:  
900 Observations of fluorescent aerosol–cloud interactions in the free troposphere at the High-Altitude Research Sta-  
901 tion Jungfraujoch, *Atmos. Chem. Phys.*, 15(19), 26067–26088, <https://doi.org/10.5194/acp-16-2273-2016>, 2016.
- 902 Crouzy, B., Stella, M., Konzelmann, T., Calpini, B. and Clot, B.: All-optical automatic pollen identification: Towards an  
903 operational system, *Atmos. Environ.*, 140, 202–212, doi:http://dx.doi.org/10.1016/j.atmosenv.2016.05.062, 2016.
- 904 Deepak, A. and Vali, G.: *The International Global Aerosol Program (IGAP) plan: Overview (Vol. 1)*, A. Deepak Pub.,  
905 1991.
- 906 DeRose, P. C.: *Standard guide to fluorescence: Instrument calibration and validation*, US Department of Commerce,  
907 Technology Administration, National Institute of Standards and Technology., 2007.
- 908 DeRose, P. C., Early, E. A. and Kramer, G. W.: Qualification of a fluorescence spectrometer for measuring true  
909 fluorescence spectra, *Rev. Sci. Instrum.*, 78(3), 33107, <https://doi.org/10.1063/1.2715952>, 2007.

910 Després, V. R., Huffman, J. A., Burrows, S. M., Hoose, C., Safatov, A. S., Buryak, G., Fröhlich-Nowoisky, J., Elbert, W.,  
911 Andreae, M. O., Pöschl, U. and Jaenicke, R.: Primary biological aerosol particles in the atmosphere: A review,  
912 *Tellus, Ser. B Chem. Phys. Meteorol.*, 64, doi:10.3402/tellusb.v64i0.15598, 2012.

913 Fennelly, M. J., Sewell, G., Prentice, M. B., O'Connor, D. J. and Sodeau, J. R.: The use of real-time fluorescence  
914 instrumentation to monitor ambient primary biological aerosol particles (PBAP), *Atmosphere (Basel)*., 9(1), 1,  
915 <https://doi.org/10.3390/atmos9010001>, 2017.

916 Fernández-Rodríguez, S., Tormo-Molina, R., Lemonis, N., Clot, B., O'Connor, D. J. and Sodeau, J. R.: Comparison of  
917 fungal spores concentrations measured with wideband integrated bioaerosol sensor and Hirst methodology,  
918 *Atmos. Environ.*, 175, 1–14, <https://doi.org/10.1016/j.atmosenv.2017.11.038>, 2018.

919 Foot, V. E., Kaye, P. H., Stanley, W. R., Barrington, S. J., Gallagher, M. and Gabey, A.: Low-cost real-time multiparameter  
920 bio-aerosol sensors, *Proc. SPIE*, 7116, 71160I–71160I–12, doi:10.1117/12.800226, 2008.

921 French, C. S., Smith, J. H. C., Virgin, H. I. and Airth, R. L.: Fluorescence-spectrum curves of chlorophylls, pheophytins,  
922 phycoerythrins, phycocyanins and hypericin., *Plant Physiol.*, 31(5), 369, 1956.

923 Fröhlich-Nowoisky, J., Kampf, C. J., Weber, B., Huffman, J. A., Pöhlker, C., Andreae, M. O., Lang-Yona, N., Burrows,  
924 S. M., Gunthe, S. S., Elbert, W., Su, H., Hoor, P., Thines, E., Hoffmann, T., Després, V. R. and Pöschl, U.:  
925 Bioaerosols in the earth system: Climate, health, and ecosystem interactions, *Atmos. Res.*, 182, 346–376,  
926 <https://doi.org/10.1016/j.atmosres.2016.07.018>, 2016.

927 Fuzzi, S., Andreae, M. O., Huebert, B. J., Kulmala, M., Bond, T. C., Boy, M., Doherty, S. J., Guenther, A., Kanakidou,  
928 M., Kawamura, K., Kerminen, V.-M., Lohmann, U., Russell, L. M. and Pöschl, U.: Critical assessment of the  
929 current state of scientific knowledge, terminology, and research needs concerning the role of organic aerosols in  
930 the atmosphere, climate, and global change, *Atmos. Chem. Phys.*, 6(7), 2017–2038, doi:10.5194/acp-6-2017-  
931 2006, 2006.

932 Gabey, A. M., Gallagher, M. W., Whitehead, J., Dorsey, J. R., Kaye, P. H. and Stanley, W. R.: Measurements and  
933 comparison of primary biological aerosol above and below a tropical forest canopy using a dual channel  
934 fluorescence spectrometer, *Atmos. Chem. Phys.*, 10(10), 4453–4466, doi:10.5194/acp-10-4453-2010, 2010.

935 Gabey, A. M., Vaitilingom, M., Freney, E., Boulon, J., Sellegri, K., Gallagher, M. W., Crawford, I. P., Robinson, N. H.,  
936 Stanley, W. R. and Kaye, P. H.: Observations of fluorescent and biological aerosol at a high-altitude site in central  
937 France, *Atmos. Chem. Phys.*, 13(15), 7415–7428, doi:10.5194/acp-13-7415-2013, 2013.

938 Gosselin, M. I., Rathnayake, C. M., Crawford, I. P., Pöhlker, C., Fröhlich-Nowoisky, J., Schmer, B., Després, V. R.,  
939 Engling, G., Gallagher, M., Stone, E., Pöschl, U., and Huffman, J. A.: Fluorescent bioaerosol particle, molecular  
940 tracer, and fungal spore concentrations during dry and rainy periods in a semi-arid forest, *Atmos. Chem. Phys.*,  
941 16(23), 15165–15184, <https://doi.org/10.5194/acp-16-15165-2016>, 2016.

942 Guilbault, G. G.: *Practical fluorescence (Vol. 3)*, CRC Press., 1990.

943 Hairston, P. P., Ho, J. and Quant, F. R.: Design of an instrument for real-time detection of bioaerosols using simultaneous  
944 measurement of particle aerodynamic size and intrinsic fluorescence, *J. Aerosol Sci.*, 28(3), 471–482,  
945 doi:10.1016/S0021-8502(96)00448-X, 1997.

946 Healy, D. A., O'Connor, D. J., Burke, A. M. and Sodeau, J. R.: A laboratory assessment of the Waveband Integrated  
947 Bioaerosol Sensor (WIBS-4) using individual samples of pollen and fungal spore material, *Atmos. Environ.*, 60,  
948 534–543, doi:10.1016/j.atmosenv.2012.06.052, 2012.

949 Healy, D. A., Huffman, J. A., O'Connor, D. J., Pöhlker, C., Pöschl, U. and Sodeau, J. R.: Ambient measurements of  
950 biological aerosol particles near Killarney, Ireland: a comparison between real-time fluorescence and microscopy  
951 techniques, *Atmos. Chem. Phys.*, 14(15), 8055–8069, doi:10.5194/acp-14-8055-2014, 2014.

952 Herbrich, S., Gehder, M., Krull, R. and Gericke, K.-H.: Label-free spatial analysis of free and enzyme-bound NAD (P) H  
953 in the presence of high concentrations of melanin, *J. Fluoresc.*, 22(1), 349–355, [https://doi.org/10.1007/s10895-](https://doi.org/10.1007/s10895-011-0965-5)  
954 011-0965-5, 2012.

955 Hernandez, M., Perring, A. E., McCabe, K., Kok, G., Granger, G. and Baumgardner, D.: Chamber catalogues of optical  
956 and fluorescent signatures distinguish bioaerosol classes, *Atmos. Meas. Tech.*, 9(7), 3283–3292,  
957 <https://doi.org/10.5194/amt-9-3283-2016>, 2016.

958 Hill, S. C., Pinnick, R. G., Niles, S., Pan, Y., Holler, S., Chang, R. K., Bottiger, J., Chen, B. T., Orr, C. and Feather, G.:  
959 Real-time measurement of fluorescence spectra from single airborne biological particles, *F. Anal. Chem. Technol.*,  
960 3(4-5), 221–239, [https://doi.org/10.1002/\(SICI\)1520-6521\(1999\)3:4/5<221::AID-FACT2>3.0.CO;2-7](https://doi.org/10.1002/(SICI)1520-6521(1999)3:4/5<221::AID-FACT2>3.0.CO;2-7), 1999.

961 Hill, S. C., Mayo, M. W. and Chang, R. K.: Fluorescence of bacteria, pollens, and naturally occurring airborne particles:  
962 excitation / emission spectra, *Army Res. Lab. Appl. Phys.*, (February), 2009.

963 Hill, S. C., Williamson, C. C., Doughty, D. C., Pan, Y.-L., Santarpia, J. L. and Hill, H. H.: Size-dependent fluorescence of  
964 bioaerosols: Mathematical model using fluorescing and absorbing molecules in bacteria, *J. Quant. Spectrosc.*  
965 *Radiat. Transf.*, 157, 54–70, doi:10.1016/j.jqsrt.2015.01.011, 2015.

966 Hinds, W. C.: *Aerosol technology: Properties. Behavior, and measurement of Airborne particles* (2nd), 1999.

967 Ho, J.: Future of biological aerosol detection, *Anal. Chim. Acta*, 457(1), 125–148, doi:[http://dx.doi.org/10.1016/S0003-](http://dx.doi.org/10.1016/S0003-2670(01)01592-6)  
968 2670(01)01592-6, 2002.

969 Holbrook, R. D., DeRose, P. C., Leigh, S. D., Rukhin, A. L. and Heckert, N. A.: Excitation–emission matrix fluorescence  
970 spectroscopy for natural organic matter characterization: a quantitative evaluation of calibration and spectral  
971 correction procedures, *Appl. Spectrosc.*, 60(7), 791–799, <https://doi.org/10.1366/000370206777886973>, 2006.

972 Huffman, J. A. and Santarpia, J.: Online techniques for quantification and characterization of biological aerosols,  
973 *Microbiol. Aerosols*, 83–114, 2017.

974 Huffman, J. A., Treutlein, B. and Pöschl, U.: Fluorescent biological aerosol particle concentrations and size distributions  
975 measured with an Ultraviolet Aerodynamic Particle Sizer (UV-APS) in Central Europe, *Atmos. Chem. Phys.*,  
976 10(7), 3215–3233, doi:10.5194/acp-10-3215-2010, 2010.

977 Huffman, J. A., Sinha, B., Garland, R. M., Snee-Pollmann, A., Gunthe, S. S., Artaxo, P., Martin, S. T., Andreae, M. O. and  
978 Pöschl, U.: Size distributions and temporal variations of biological aerosol particles in the Amazon rainforest  
979 characterized by microscopy and real-time UV-APS fluorescence techniques during AMAZE-08, *Atmos. Chem.*  
980 *Phys.*, 12, 11997–12019, doi:10.5194/acp-12-11997-2012, 2012.

981 Huffman, J. A., Prenni, A. J., Demott, P. J., Pöhlker, C., Mason, R. H., Robinson, N. H., Fröhlich-Nowoisky, J., Tobo, Y.,  
982 Després, V. R., Garcia, E., Gochis, D. J., Harris, E., Müller-Germann, I., Ruzene, C., Schmer, B., Sinha, B., Day,  
983 D. A., Andreae, M. O., Jimenez, J. L., Gallagher, M., Kreidenweis, S. M., Bertram, A. K. and Pöschl, U.: High  
984 concentrations of biological aerosol particles and ice nuclei during and after rain, *Atmos. Chem. Phys.*, 13, 6151–  
985 6164, doi:10.5194/acp-13-6151-2013, 2013.

986 Hunter, A. J. R., Morency, J. R., Senior, C. L., Davis, S. J. and Fraser, M. E.: Continuous emissions monitoring using  
987 spark-induced breakdown spectroscopy, *J. Air Waste Manage. Assoc.*, 50(1), 111–117,  
988 <https://doi.org/10.1080/10473289.2000.10463982>, 2000.

989 Jaenicke, R.: Abundance of cellular material and proteins in the atmosphere., *Science*, 308, 73,  
990 doi:10.1126/science.1106335, 2005.

991 Jeys, T. H., Herzog, W. D., Hybl, J. D., Czerwinski, R. N. and Sanchez, A.: Advanced trigger development, *Lincoln Lab.*  
992 *J.*, 17(1), 29–62, 2007.

993 Johnson, I. D., Thomas, E. W. and Cundall, R. B.: Fluorescence solvatochromism of nitrodiphenylhexatrienes, *J. Chem.*

994 Soc. Faraday Trans. 2 Mol. Chem. Phys., 81(9), 1303–1315, doi: 10.1039/F29858101303, 1985.

995 Jonsson, P. and Tjärnhage, T.: Trends in Biological Detection BT - Bioaerosol detection technologies, edited by P. Jonsson,  
996 G. Olofsson, and T. Tjärnhage, pp. 317–322, Springer New York, New York, NY., 2014.

997 Kanaani, H., Hargreaves, M., Ristovski, Z. and Morawska, L.: Performance assessment of UVAPS: Influence of fungal  
998 spore age and air exposure, *J. Aerosol Sci.*, 38(1), 83–96, doi:10.1016/j.jaerosci.2006.10.003, 2007.

999 Kaye, P. H., Eyles, N. A., Ludlow, I. K. and Clark, J. M.: An instrument for the classification of airborne particles on the  
1000 basis of size, shape, and count frequency, *Atmos. Environ. Part A. Gen. Top.*, 25(3–4), 645–654,  
1001 [https://doi.org/10.1016/0960-1686\(91\)90062-C](https://doi.org/10.1016/0960-1686(91)90062-C), 1991.

1002 Kaye, P. H., Alexander-Buckley, K., Hirst, E., Saunders, S. and Clark, J. M.: A real-time monitoring system for airborne  
1003 particle shape and size analysis, *J. Geophys. Res. Atmos.*, 101(D14), 19215–19221,  
1004 <https://doi.org/10.1029/96JD00228>, 1996.

1005 Kaye, P. H., Barton, J. E., Hirst, E. and Clark, J. M.: Simultaneous light scattering and intrinsic fluorescence measurement  
1006 for the classification of airborne particles., *Appl. Opt.*, 39(21), 3738–3745, doi:10.1364/AO.39.003738, 2000.

1007 Kaye, P. H., Stanley, W. R., Hirst, E., Foot, E. V., Baxter, K. L. and Barrington, S. J.: Single particle multichannel bio-  
1008 aerosol fluorescence sensor, *Opt. Express*, 13(10), 3583–3593, doi:10.1364/OPEX.13.003583, 2005.

1009 Khalaji, M., Roshanzadeh, B., Mansoori, A., Taefi, N. and Tavassoli, S. H.: Continuous dust monitoring and analysis by  
1010 spark induced breakdown spectroscopy, *Opt. Lasers Eng.*, 50(2), 110–113, <https://doi.org/10.1016/j.optlas-eng.2011.10.009>, 2012.

1012 Kiselev, D., Bonacina, L. and Wolf, J.-P.: Individual bioaerosol particle discrimination by multi-photon excited  
1013 fluorescence, *Opt. Express*, 19(24), 24516–24521, <https://doi.org/10.1364/OE.19.024516>, 2011.

1014 Kiselev, D., Bonacina, L. and Wolf, J.-P.: A flash-lamp based device for fluorescence detection and identification of  
1015 individual pollen grains, *Rev. Sci. Instrum.*, 84(3), 33302, <https://doi.org/10.1063/1.4793792>, 2013.

1016 Könemann, T., Savage, N. J., Huffman, J. A. and Pöhlker, C.: Characterization of steady-state fluorescence properties of  
1017 polystyrene latex spheres using off-and online spectroscopic methods, *Atmos. Meas. Tech.*, 11(7), 3987–4003,  
1018 <https://doi.org/10.5194/amt-11-3987-2018>, 2018.

1019 Lakowicz, J. R.: Principles of fluorescence spectroscopy, (1999), 2004.

1020 Li, J. K., Asali, E. C., Humphrey, A. E. and Horvath, J. J.: Monitoring cell concentration and activity by multiple excitation  
1021 fluorometry, *Biotechnol. Prog.*, 7(1), 21–27, doi:10.1021/bp00007a004, 1991.

1022 Lorenz, L.: Lysbevægelsen i og uden for en af plane Lysbølger belyst Kugle, na., 1890.

1023 Ma, Y., Wang, Z., Yang, D., Diao, Y., Wang, W., Zhang, H., Zhu, W. and Zheng, J.: On-line measurement of fluorescent  
1024 aerosols near an industrial zone in the Yangtze River Delta region using a wideband integrated bioaerosol  
1025 spectrometer, *Sci. Total Environ.*, 656, 447–457, <https://doi.org/10.1016/j.scitotenv.2018.11.370>, 2019.

1026 Madelin, T. M.: Fungal aerosols: A review, *J. Aerosol Sci.*, 25, 1405–1412, doi:10.1016/0021-8502(94)90216-X, 1994.

1027 Mie, G.: Considerations on the optics of turbid media, especially metal sols, *Ann. Phys*, 25, 377–442,  
1028 <https://doi.org/10.1002/andp.19083300302>, 1908.

1029 Moran-Zuloaga, D., Ditas, F., Walter, D., Saturno, J., Brito, J., Carbone, S., Chi, X., Hrabě de Angelis, I., Baars, H., Godoi,  
1030 R. H. M., Heese, B., Holanda, B. A., Lavrič, J. V., Martin, S. T., Ming, J., Pöhlker, M. L., Ruckteschler, N., Su,  
1031 H., Wang, Y., Wang, Q., Wang, Z., Weber, B., Wolff, S., Artaxo, P., Pöschl, U., Andreae, M. O., and Pöhlker,  
1032 C.: Long-term study on coarse mode aerosols in the Amazon rain forest with the frequent intrusion of Saharan  
1033 dust plumes, *Atmos. Chem. Phys.*, 18, 10055–10088, <https://doi.org/10.5194/acp-18-10055-2018>, 2018.

1034 Nasir, Z., Rolph, C., Collins, S., Stevenson, D., Gladding, T., Hayes, E., Williams, B., Khera, S., Jackson, S. and Bennett,  
1035 A.: A controlled study on the characterisation of bioaerosols emissions from compost, *Atmosphere (Basel)*, 9(10),

1036 379, <https://doi.org/10.3390/atmos9100379>, 2018.

1037 O'Connor, D. J., Healy, D. A. and Sodeau, J. R.: The on-line detection of biological particle emissions from selected  
1038 agricultural materials using the WIBS-4 (Waveband Integrated Bioaerosol Sensor) technique, *Atmos. Environ.*,  
1039 80, 415–425, <https://doi.org/10.1016/j.atmosenv.2013.07.051>, 2013.

1040 O'Connor, D. J., Lovera, P., Iacopino, D., O'Riordan, A., Healy, D. A. and Sodeau, J. R.: Using spectral analysis and  
1041 fluorescence lifetimes to discriminate between grass and tree pollen for aerobiological applications, *Anal.*  
1042 *Methods*, 6(6), 1633–1639, doi: 10.1039/C3AY41093E, 2014.

1043 Pan, Y.-L., Hartings, J., Pinnick, R. G., Hill, S. C., Halverson, J. and Chang, R. K.: Single-particle fluorescence spectrometer  
1044 for ambient aerosols, *Aerosol Sci. Technol.*, 37(8), 628–639, <https://doi.org/10.1080/02786820300904>, 2003.

1045 Pan, Y.-L., Hill, S. C., Pinnick, R. G., Huang, H., Bottiger, J. R. and Chang, R. K.: Fluorescence spectra of atmospheric  
1046 aerosol particles measured using one or two excitation wavelengths: Comparison of classification schemes  
1047 employing different emission and scattering results, *Opt. Express*, 18(12), 12436–12457,  
1048 doi:10.1364/OE.18.012436, 2010.

1049 Pan, Y.-L.: Detection and characterization of biological and other organic-carbon aerosol particles in atmosphere using  
1050 fluorescence, *J. Quant. Spectrosc. Radiat. Transf.*, 150, 12–35, doi:10.1016/j.jqsrt.2014.06.007, 2015.

1051 Pelling, A. E., Sehati, S., Gralla, E. B., Valentine, J. S. and Gimzewski, J. K.: Local nanomechanical motion of the cell  
1052 wall of *Saccharomyces cerevisiae*, *Science* (80-. ), 305(5687), 1147–1150, doi: 10.1126/science.1097640, 2004.

1053 Perring, A. E., Schwarz, J. P., Baumgardner, D., Hernandez, M. T., Spracklen, D. V., Heald, C. L., Gao, R. S., Kok, G.,  
1054 McMeeking, G. R., McQuaid, J. B. and Fahey, D. W.: Airborne observations of regional variation in fluorescent  
1055 aerosol across the United States, *J. Geophys. Res. Atmos.*, 120(3), 1153–1170, doi:10.1002/2014JD022495, 2015.

1056 Pinnick, R. G., Hill, S. C., Pan, Y. -L. and Chang, R. K.: Fluorescence spectra of atmospheric aerosol at Adelphi, Maryland,  
1057 USA: Measurement and classification of single particles containing organic carbon, *Atmos. Environ.*, 38(11),  
1058 1657–1672, doi:10.1016/j.atmosenv.2003.11.017, 2004.

1059 Pöhlker, C., Huffman, J. A. and Pöschl, U.: Autofluorescence of atmospheric bioaerosols – fluorescent biomolecules and  
1060 potential interferences, *Atmos. Meas. Tech.*, 5(1), 37–71, doi:10.5194/amt-5-37-2012, 2012.

1061 Pöhlker, C., Huffman, J. A., Förster, J.-D. and Pöschl, U.: Autofluorescence of atmospheric bioaerosols: spectral  
1062 fingerprints and taxonomic trends of pollen, *Atmos. Meas. Tech.*, 6(12), 3369–3392, [https://doi.org/10.5194/amt-](https://doi.org/10.5194/amt-6-3369-2013)  
1063 [6-3369-2013](https://doi.org/10.5194/amt-6-3369-2013), 2013.

1064 Pöschl, U.: Atmospheric aerosols: Composition, transformation, climate and health effects, *Angew. Chemie Int. Ed.*,  
1065 44(46), 7520–7540, doi:10.1002/anie.200501122, 2005.

1066 Pöschl, U. and Shiraiwa, M.: Multiphase chemistry at the atmosphere–biosphere interface influencing climate and public  
1067 health in the Anthropocene, *Chem. Rev.*, 115(10), 4440–4475, doi:10.1021/cr500487s, 2015.

1068 Reid, J. S., Jonsson, H. H., Maring, H. B., Smirnov, A., Savoie, D. L., Cliff, S. S., Reid, E. A., Livingston, J. M., Meier,  
1069 M. M. and Dubovik, O.: Comparison of size and morphological measurements of coarse mode dust particles from  
1070 Africa, *J. Geophys. Res. Atmos.*, 108(D19), <https://doi.org/10.1029/2002JD002485>, 2003.

1071 Reponen, T., Grinshpun, S. A., Conwell, K. L., Wiest, J. and Anderson, M.: Aerodynamic versus physical size of spores:  
1072 measurement and implication for respiratory deposition, *Grana*, 40(3), 119–125,  
1073 <https://doi.org/10.1080/00173130152625851>, 2001.

1074 Richards-Kortum, R. and Sevick-Muraca, E.: Quantitative optical spectroscopy for tissue diagnosis, *Annu. Rev. Phys.*  
1075 *Chem.*, 47(1), 555–606, <https://doi.org/10.1146/annurev.physchem.47.1.555>, 1996.

1076 Rijgersberg, C. P., Van Grondelle, R. and Amesz, J.: Energy transfer and bacteriochlorophyll fluorescence in purple  
1077 bacteria at low temperature, *Biochim. Biophys. Acta (BBA)-Bioenergetics*, 592(1), 53–64,

1078 [https://doi.org/10.1016/0005-2728\(80\)90113-9](https://doi.org/10.1016/0005-2728(80)90113-9), 1980.

1079 Robinson, E. S., Gao, R.-S., Schwarz, J. P., Fahey, D. W. and Perring, A. E.: Fluorescence calibration method for single-  
1080 particle aerosol fluorescence instruments, *Atmos. Meas. Tech.*, 10(5), 1755–1768, [https://doi.org/10.5194/amt-](https://doi.org/10.5194/amt-10-1755-2017)  
1081 [10-1755-2017](https://doi.org/10.5194/amt-10-1755-2017), 2017.

1082 Robinson, N. H., Allan, J. D., Huffman, J. A., Kaye, P. H., Foot, V. E. and Gallagher, M. W.: Cluster analysis of WIBS  
1083 single-particle bioaerosol data, *Atmos. Meas. Tech.*, <https://doi.org/10.5194/amt-6-337-2013>, 2013.

1084 Ruske, S., Topping, D. O., Foot, V. E., Kaye, P. H., Stanley, W., Crawford, I. P., Morse, A. and Gallagher, M. W.:  
1085 Evaluation of machine learning algorithms for classification of primary biological aerosol using a new UV-LIF  
1086 spectrometer, *Atmos. Meas. Tech.*, <https://doi.org/10.5194/amt-10-695-2017>, 2017.

1087 Saari, S. E., Putkiranta, M. J. and Keskinen, J.: Fluorescence spectroscopy of atmospherically relevant bacterial and fungal  
1088 spores and potential interferences, *Atmos. Environ.*, 71, 202–209,  
1089 [doi:http://dx.doi.org/10.1016/j.atmosenv.2013.02.023](http://dx.doi.org/10.1016/j.atmosenv.2013.02.023), 2013.

1090 Saari, S. E., Reponen, T. and Keskinen, J.: Performance of two fluorescence-based real-time bioaerosol detectors: BioScout  
1091 vs. UVAPS, *Aerosol Sci. Technol.*, 48(4), 371–378, [doi:10.1080/02786826.2013.877579](https://doi.org/10.1080/02786826.2013.877579), 2014.

1092 Savage, N. J., Krentz, C. E., Könemann, T., Han, T. T., Mainelis, G., Pöhlker, C. and Huffman, J. A.: Systematic  
1093 characterization and fluorescence threshold strategies for the wideband integrated bioaerosol sensor (WIBS) using  
1094 size-resolved biological and interfering particles, *Atmos. Meas. Tech.*, 10(11), 4279–4302, [doi:10.5194/amt-10-](https://doi.org/10.5194/amt-10-4279-2017)  
1095 [4279-2017](https://doi.org/10.5194/amt-10-4279-2017), 2017.

1096 Savage, N. J. and Huffman, J. A.: Evaluation of a hierarchical agglomerative clustering method applied to WIBS laboratory  
1097 data for improved discrimination of biological particles by comparing data preparation techniques, *Atmos. Meas.*  
1098 *Tech.*, 11(8), 4929–4942, <https://doi.org/10.5194/amt-11-4929-2018>, 2018.

1099 Schmauss, A. and Wigand, A.: *Die Atmosphäre als Kolloid*, Vieweg+Teubner Verlag, Wiesbaden., 1929.

1100 Schmidt, M. S. and Bauer, A. J. R.: Preliminary correlations of feature strength in spark-induced breakdown spectroscopy  
1101 of bioaerosols with concentrations measured in laboratory analyses, *Appl. Opt.*, 49(13), C101–C109,  
1102 <https://doi.org/10.1364/AO.49.00C101>, 2010.

1103 Schumacher, C. J., Pöhlker, C., Aalto, P., Hiltunen, V., Petäjä, T., Kulmala, M., Pöschl, U. and Huffman, J. A.: Seasonal  
1104 cycles of fluorescent biological aerosol particles in boreal and semi-arid forests of Finland and Colorado, *Atmos.*  
1105 *Chem. Phys.*, 13(23), 11987–12001, [doi:10.5194/acp-13-11987-2013](https://doi.org/10.5194/acp-13-11987-2013), 2013.

1106 Shaw, S. L., Yeh, E., Bloom, K. and Salmon, E. D.: Imaging green fluorescent protein fusion proteins in *Saccharomyces*  
1107 *cerevisiae*, *Curr. Biol.*, 7(9), 701–704, [https://doi.org/10.1016/S0960-9822\(06\)00299-5](https://doi.org/10.1016/S0960-9822(06)00299-5), 1997.

1108 Sinski, J. F. and Exner, J.: Concentration dependence in the spectra of polycyclic aromatic hydrocarbon mixtures by front-  
1109 surface fluorescence analysis, *Appl. Spectrosc.*, 61(9), 970–977, <https://doi.org/10.1366/000370207781746026>,  
1110 2007.

1111 Sivaprakasam, V., Lin, H.-B., Huston, A. L. and Eversole, J. D.: Spectral characterization of biological aerosol particles  
1112 using two-wavelength excited laser-induced fluorescence and elastic scattering measurements, *Opt. Express*,  
1113 19(7), 6191–6208, [doi:10.1364/OE.19.006191](https://doi.org/10.1364/OE.19.006191), 2011.

1114 Sodeau, J. R. and O'Connor, D. J.: Chap. 16 – Bioaerosol monitoring of the atmosphere for occupational and environmental  
1115 purposes, in: *Compr. Anal. Chem.*, 73, 391–420, <http://dx.doi.org/10.1016/bs.coac.2016.02.012>, 2016.

1116 Stanley, W. R., Kaye, P. H., Foot, V. E., Barrington, S. J., Gallagher, M. and Gabey, A.: Continuous bioaerosol monitoring  
1117 in a tropical environment using a UV fluorescence particle spectrometer, *Atmos. Sci. Lett.*, 12(2), 195–199,  
1118 [doi:10.1002/asl.310](https://doi.org/10.1002/asl.310), 2011.

1119 Swanson, B. E. and Huffman, J. A.: Development and characterization of an inexpensive single-particle fluorescence



1120 spectrometer for bioaerosol monitoring, *Opt. Express*, 26(3), 3646–3660, <https://doi.org/10.1364/OE.26.003646>,  
1121 2018.

1122 Toprak, E. and Schnaiter, M.: Fluorescent biological aerosol particles measured with the Waveband Integrated Bioaerosol  
1123 Sensor WIBS-4: laboratory tests combined with a one year field study, *Atmos. Chem. Phys.*, 13(1), 225–243,  
1124 [doi:10.5194/acp-13-225-2013](https://doi.org/10.5194/acp-13-225-2013), 2013.

1125 Twohy, C. H., McMeeking, G. R., DeMott, P. J., McCluskey, C. S., Hill, T. C. J., Burrows, S. M., Kulkarni, G. R., Tanarhte,  
1126 M., Kafle, D. N. and Toohey, D. W.: Abundance of fluorescent biological aerosol particles at temperatures  
1127 conducive to the formation of mixed-phase and cirrus clouds, *Atmos. Chem. Phys.*, 16(13), 8205–8225,  
1128 <https://doi.org/10.5194/acp-16-8205-2016>, 2016.

1129 Van Grondelle, R., Hunter, C. N., Bakker, J. G. C. and Kramer, H. J. M.: Size and structure of antenna complexes of  
1130 photosynthetic bacteria as studied by singlet-singlet quenching of the bacteriochlorophyll fluorescence yield,  
1131 *Biochim. Biophys. Acta (BBA)-Bioenergetics*, 723(1), 30–36, [https://doi.org/10.1016/0005-2728\(83\)90005-1](https://doi.org/10.1016/0005-2728(83)90005-1),  
1132 1983.

1133 Von der Weiden, S. L., Drewnick, F. and Borrmann, S.: Particle Loss Calculator—a new software tool for the assessment  
1134 of the performance of aerosol inlet systems, *Atmos. Meas. Tech*, 2(2), 479–494, <https://doi.org/10.5194/amt-2-479-2009>, 2009.

1136 Welschmeyer, N. A.: Fluorometric analysis of chlorophyll a in the presence of chlorophyll b and pheopigments, *Limnol.*  
1137 *Oceanogr.*, 39(8), 1985–1992, <https://doi.org/10.4319/lo.1994.39.8.1985>, 1994.

1138 Yao, M.: Bioaerosol: A bridge and opportunity for many scientific research fields, *J. Aerosol Sci.*, 115, 108–112,  
1139 <https://doi.org/10.1016/j.jaerosci.2017.07.010>, 2018.

1140 Ziemba, L. D., Beyersdorf, A. J., Chen, G., Corr, C. A., Crumeyrolle, S. N., Diskin, G., Hudgins, C., Martin, R., Mikoviny,  
1141 T. and Moore, R.: Airborne observations of bioaerosol over the Southeast United States using a wideband  
1142 integrated bioaerosol sensor, *J. Geophys. Res. Atmos.*, 121(14), 8506–8524,  
1143 <https://doi.org/10.1002/2015JD024669>, 2016.

1144

1145 **Appendix A:** List of acronyms and symbols.

<b>Acronym/Symbol</b>	<b>Description</b>
<b>AF</b>	Asymmetry factor
<b>APC</b>	Airborne Particle Classifier
<b>CCD</b>	Charge-coupled device
<b>DMT</b>	Droplet Measurement Technologies
<b>EEM</b>	Excitation-emission matrix
<b>EM</b>	Emission
<b>EX</b>	Excitation
<b>IR</b>	Infrared
<b>LIF</b>	Light-induced fluorescence
<b><i>N</i></b>	Particle number concentration ( $\text{cm}^{-3}$ )
<b><i>N</i><sub>T,c</sub></b>	<i>N</i> of total coarse particles (1-20 $\mu\text{m}$ )
<b><i>N</i><sub>F,c(n<math>\sigma</math>)</sub></b>	<i>N</i> of fluorescent coarse particles (1-20 $\mu\text{m}$ ) at 1, 3, or 6 $\sigma$
<b>NAD</b>	Nicotinamide adenine dinucleotide
<b>NAD(P)H</b>	Nicotinamide adenine dinucleotide and nicotinamide adenine dinucleotide phosphate
<b>NIST</b>	National institute of standards and technology
<b>PBAP</b>	Primary biological aerosol particles
<b>PMT</b>	Photomultiplier tube
<b>PAH</b>	Polycyclic aromatic hydrocarbons
<b>PSL</b>	Polystyrene latex sphere
<b>PS-DVB</b>	Polystyrene-divinylbenzene
<b>SD</b>	Standard deviation
<b>SIBS</b>	Spectral intensity bioaerosol sensor
<b>SNR</b>	Signal to noise ratio
<b>TSP</b>	Total suspended particles
<b>UV</b>	Ultraviolet
<b>UV-APS</b>	Ultraviolet aerodynamic particle sizer
<b>Vis</b>	Visible light
<b>WIBS</b>	Wideband integrated bioaerosol sensor

1146

1147 **Table 1.** Lower, mean, and upper wavelength at each PMT detection channel. Nominal data accord-  
1148 ing to manufacturer Hamamatsu.

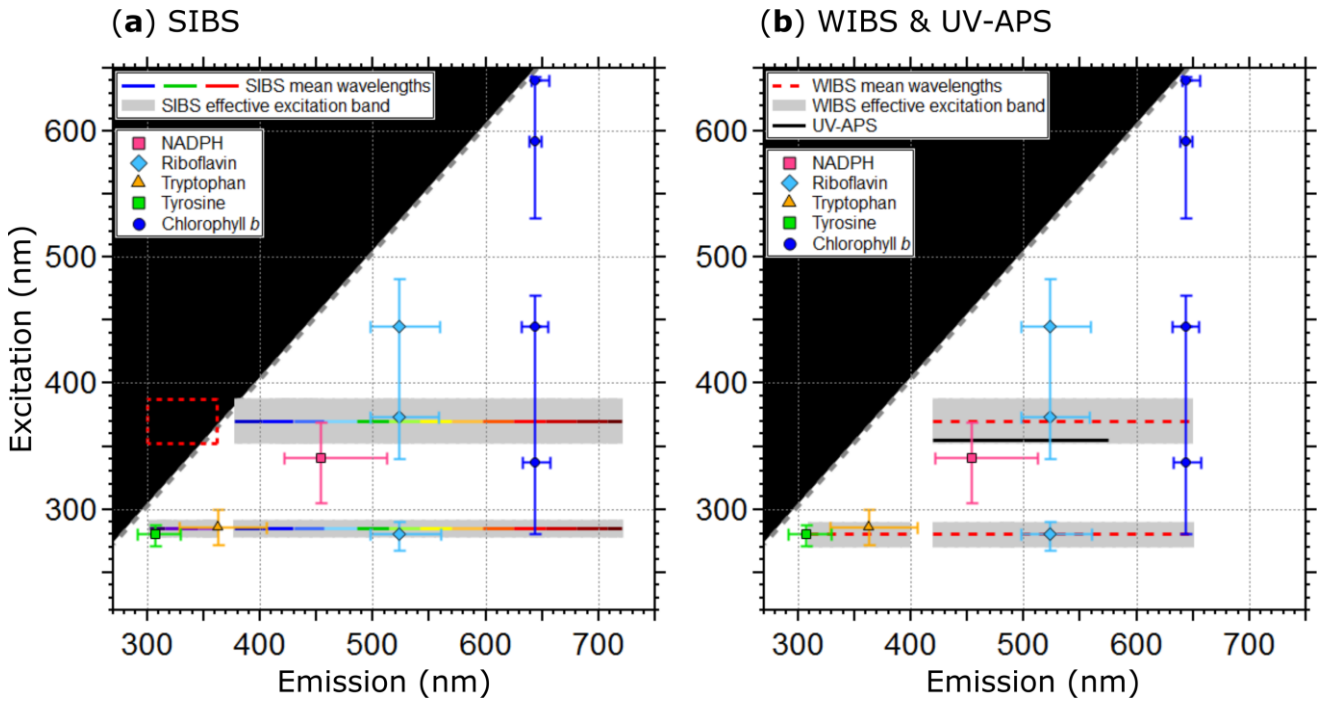
<b>Channel</b>	<b><math>\lambda_{\text{lower}}</math> (nm)</b>	<b><math>\lambda_{\text{mean}}</math> (nm)</b>	<b><math>\lambda_{\text{upper}}</math> (nm)</b>
<b>1</b>	298.2	302.2	316.2
<b>2</b>	316.6	330.6	344.6
<b>3</b>	345.0	359.0	362.5
<b>4</b>	377.5	387.3	401.3
<b>5</b>	401.5	415.6	429.7
<b>6</b>	429.8	443.8	457.8
<b>7</b>	457.9	471.9	485.9
<b>8</b>	486.0	500.0	514.0
<b>9</b>	514.0	528.0	542.0
<b>10</b>	541.9	555.9	569.9
<b>11</b>	569.7	583.7	597.7
<b>12</b>	597.4	611.4	625.4
<b>13</b>	625.0	639.0	653.0
<b>14</b>	652.8	666.5	680.2
<b>15</b>	679.9	693.9	707.9
<b>16</b>	707.1	721.1	735.1

1149 **Table 2.** Parameters and technical components of the SIBS in comparison to the WIBS-NEO and  
 1150 WIBS-4A. Data are taken from manufacturer information.

	<b>SIBS</b>	<b>WIBS-NEO</b>	<b>WIBS-4A</b>
<b>First production</b>	2015	2016	2009
<b>Measured parameters</b>	Particle size Asymmetry Factor Fluorescence spectra	Particle size Asymmetry Factor Integrated fluorescence in 3 channels	Particle size Asymmetry Factor Integrated fluorescence in 3 channels
<b>Particle size range</b>	~0.3 – 100 $\mu\text{m}$	~0.5 – 30 $\mu\text{m}$	~0.5 – 20 $\mu\text{m}$
<b>Maximum concentration</b>	$\sim 2 \times 10^4$ particles/L	$\sim 2 \times 10^4$ particles/L	$\sim 2 \times 10^4$ particles/L
<b>Fluorescence excitation</b>	$\lambda_{\text{ex}} = 285$ and $\lambda_{\text{ex}} = 370$ nm	$\lambda_{\text{ex}} = 280$ and $\lambda_{\text{ex}} = 370$ nm	$\lambda_{\text{ex}} = 280$ and $\lambda_{\text{ex}} = 370$ nm
<b>Fluorescence emission</b>	$\lambda_{\text{mean}} = 302 - 721$ nm (16-channel PMT)	$\lambda_{\text{em}} = 310-400$ nm and $\lambda_{\text{em}} = 420-650$ nm	$\lambda_{\text{em}} = 310-400$ nm and $\lambda_{\text{em}} = 420-650$ nm
<b>Flow rate</b>	Sample flow: ~0.3 l/min Sheath flow: ~2.2 l/min (re-circulating)	Sample flow: ~0.3 l/min Sheath flow: ~2.2 l/min (re-circulating)	Sample flow: ~0.3 l/min Sheath flow: ~2.2 l/min (re-circulating)
<b>Laser</b>	785 nm diode laser, 55 mW	635 nm diode laser, 15 mW	635 nm diode laser, 12 mW
<b>Pump</b>	Diaphragm pump	Diaphragm pump	Diaphragm pump
<b>Power requirements</b>	200 W, 90 - 230 VAC	150 W, 90 - 230 VAC	150 W, 90 - 230 VAC
<b>Weight (kg)</b>	20.1	12.5	13.6
<b>Dimension W x L x H (cm)</b>	42.5 x 61.5 x 23.5	45.1 x 36.2 x 24.1	30.4 x 38.2 x 17.1

1151 **Table 3.** Asymmetry factor (AF) values for reference particles. Values are based on the mean of a  
1152 Gaussian fit applied onto each particle histogram (see also Fig. 10), including  $1\sigma$  SD.

	<b>AF</b>
<b>2 <math>\mu\text{m}</math> non-fluorescent PSLs</b>	$9.9 \pm 3.6$
<b>Ultrapure water</b>	$11.9 \pm 2.9$
<b>Ammonium sulfate</b>	$13.1 \pm 8.1$
<b>Fe<sub>3</sub>O<sub>4</sub></b>	$14.4 \pm 7.4$
<b>Carbon nanotubes</b>	$21.6 \pm 12.7$



1153 **Figure 1.** Optical design and overview of excitation and emission specifications of the LIF instru-  
 1154 ments UV-APS, WIBS, and the SIBS with spectral locations of the autofluorescence modes of the  
 1155 biofluorophores tyrosine, tryptophan, NAD(P)H, riboflavin, and chlorophyll *b* (as examples). Here  
 1156 the term WIBS includes the WIBS-4A and WIBS-NEO, because both instruments use the same opti-  
 1157 cal components. Spectral properties of the emission bands of LIF instruments are illustrated as hori-  
 1158 zontal lines. The color-coded bars in (a) illustrate the spectrally resolved fluorescence detection of  
 1159 the two excitation wavelengths ( $\lambda_{\text{ex}} = 285$  and  $370$  nm) by the SIBS. The “blind spot” (white notch)  
 1160 at  $\lambda_{\text{ex}} = 285$  nm between  $\lambda_{\text{em}} = 362 - 377$  nm (a) originates from a notch optical filter, used to block  
 1161 incident light from the excitation sources. Grey dashed lines show the 1<sup>st</sup> order elastic scattering. At  
 1162  $\lambda_{\text{ex}} = 370$  nm, the detection range of the SIBS includes the spectral range where  $\lambda_{\text{em}} < \lambda_{\text{ex}}$ , for which  
 1163 fluorescence is not defined and so data within the red dashed rectangle is omitted (a). Grey bars  
 1164 indicate the effective excitation bands of optical filters used for the WIBS and SIBS (see also Sect.  
 1165 3.3 and Fig. 3). The effective excitation bands in the WIBS and SIBS occur in a spectral range span-  
 1166 ning several nanometers (up to 36 nm), in contrast to the UV-APS (black line, b), which uses a laser  
 1167 source with a defined excitation (Figure adapted from Pöhlker et al., 2012).

1168  
1169  
1170  
1171  
1172  
1173  
1174  
1175  
1176  
1177  
1178  
1179  
1180  
1181  
1182  
1183  
1184  
1185  
1186  
1187  
1188  
1189  
1190  
1191  
1192  
1193

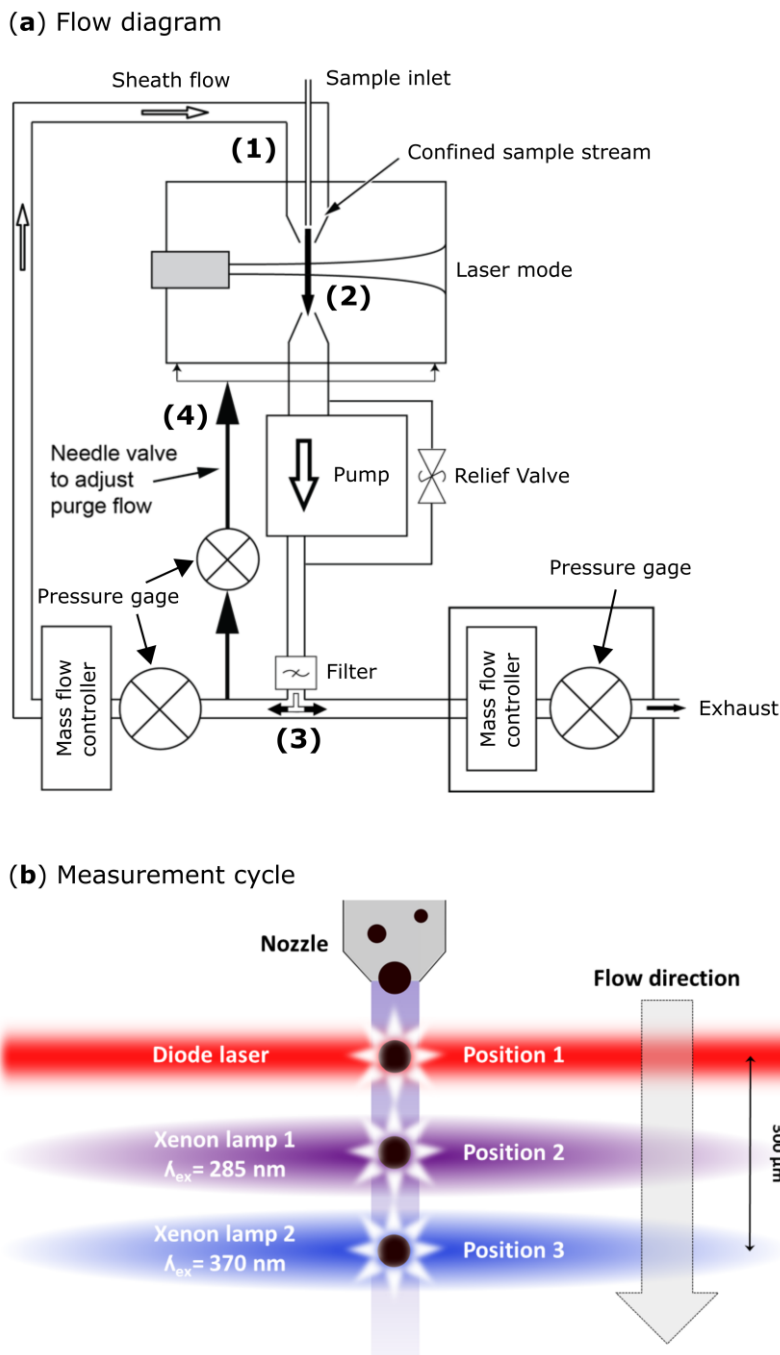
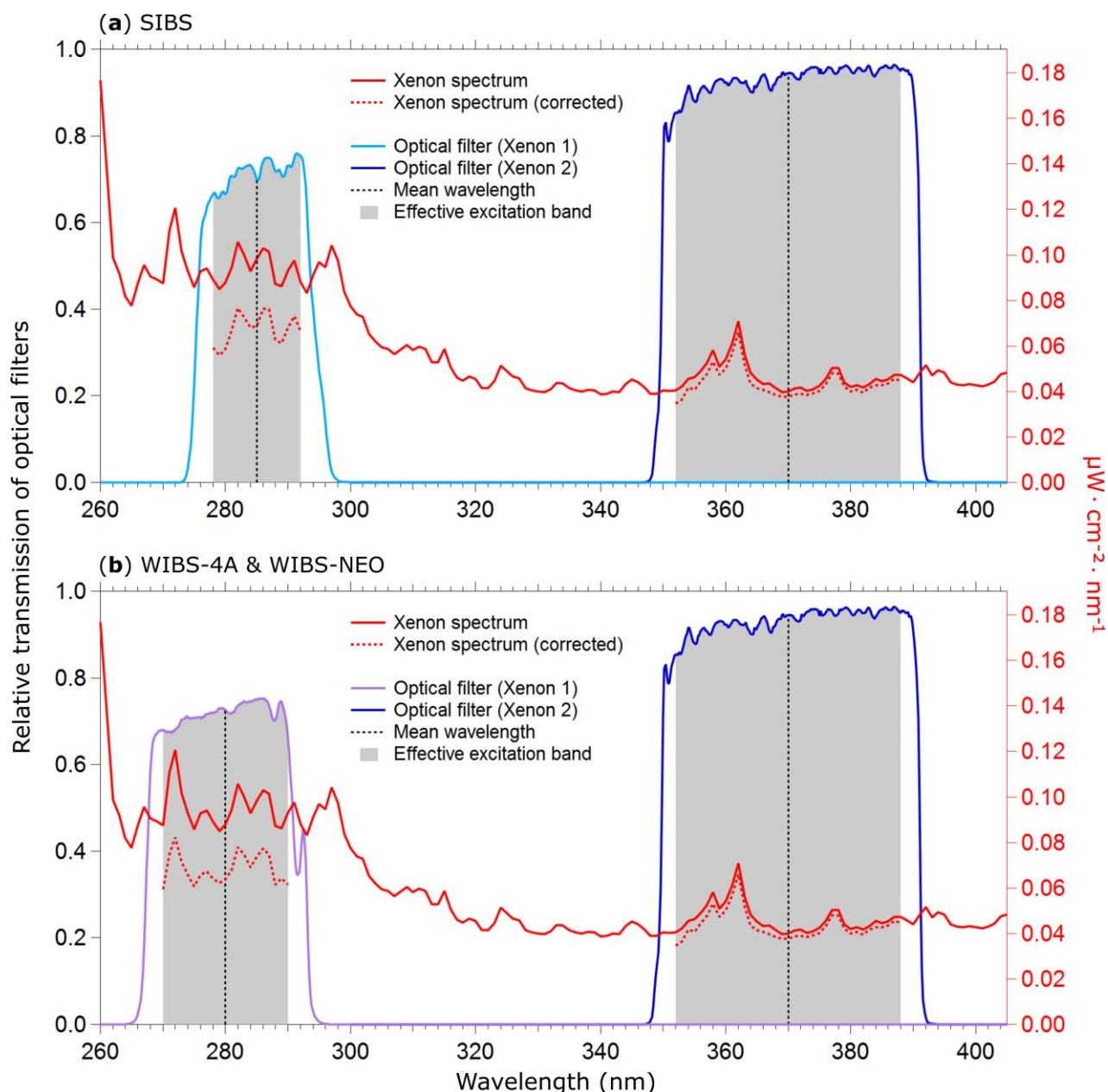


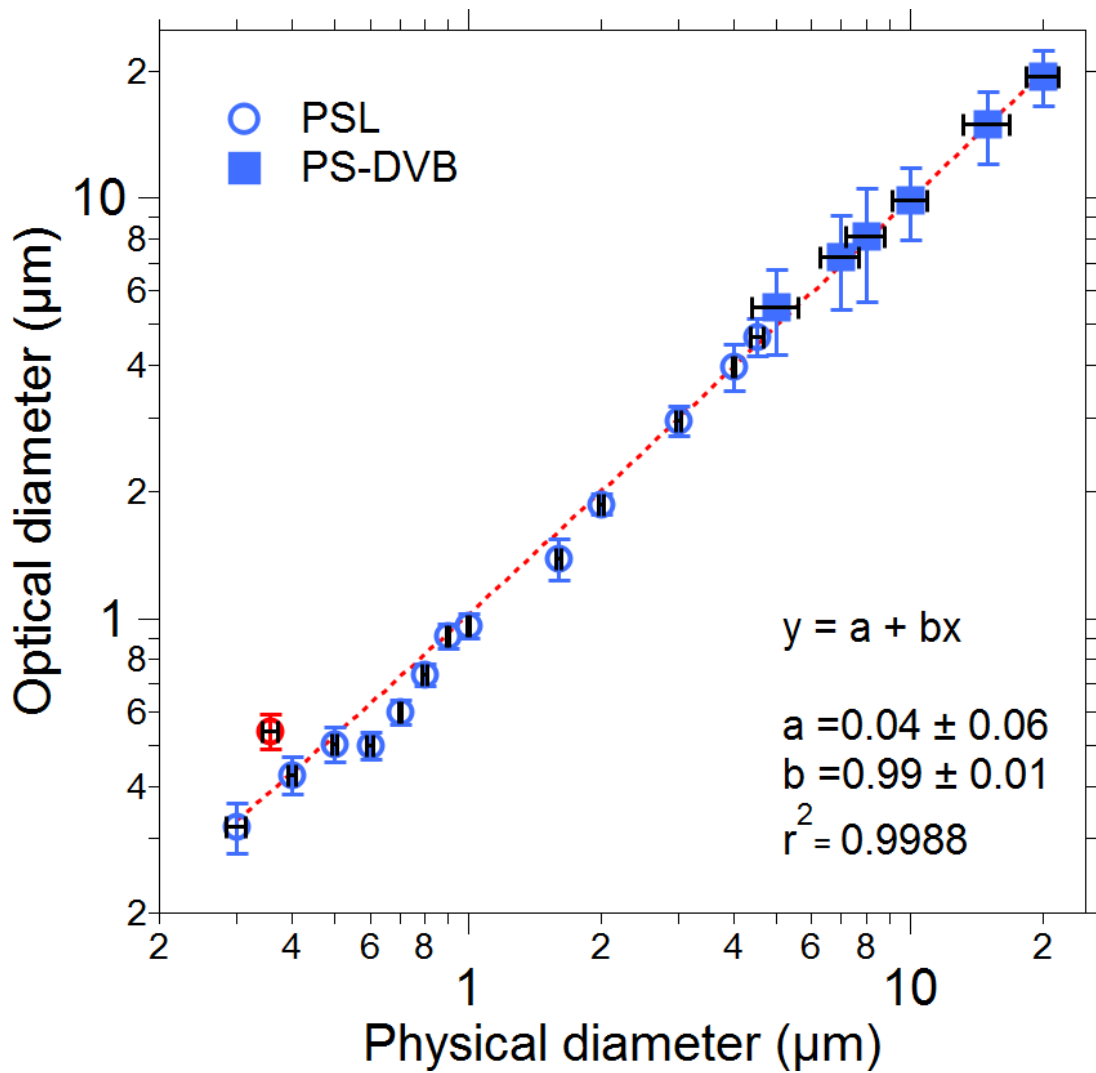
**Figure 2.** SIBS flow diagram in (a): (1) Tapered delivery nozzle. (2) Intersection of sample flow and laser beam. Sampling volume:  $\sim 0.7$  mm diameter;  $\sim 130$   $\mu\text{m}$  depth. (3) Filtered (through HEPA filter) and recirculating sheath flow. (4) Needle valve for adjusting purge flow, which constantly purges the optical cavity. SIBS measurement cycle in (b): Position 1: Particles scatter light in all directions after being illuminated by a diode laser ( $\lambda = 785$  nm). Position 2: Xenon lamp 1 is firing at  $\lambda_{ex} = 285$  nm. Position 3: Xenon lamp 2 is firing at  $\lambda_{ex} = 370$  nm. The measurement cycle from position 1 to position 3 takes  $\sim 25$   $\mu\text{s}$  over a distance of  $\sim 300$   $\mu\text{m}$ . (a) and (b): Modified, image courtesy: DMT. (b) adapted from WIBS-4A service manual (DOC-0345 Rev A), DMT; 2012).



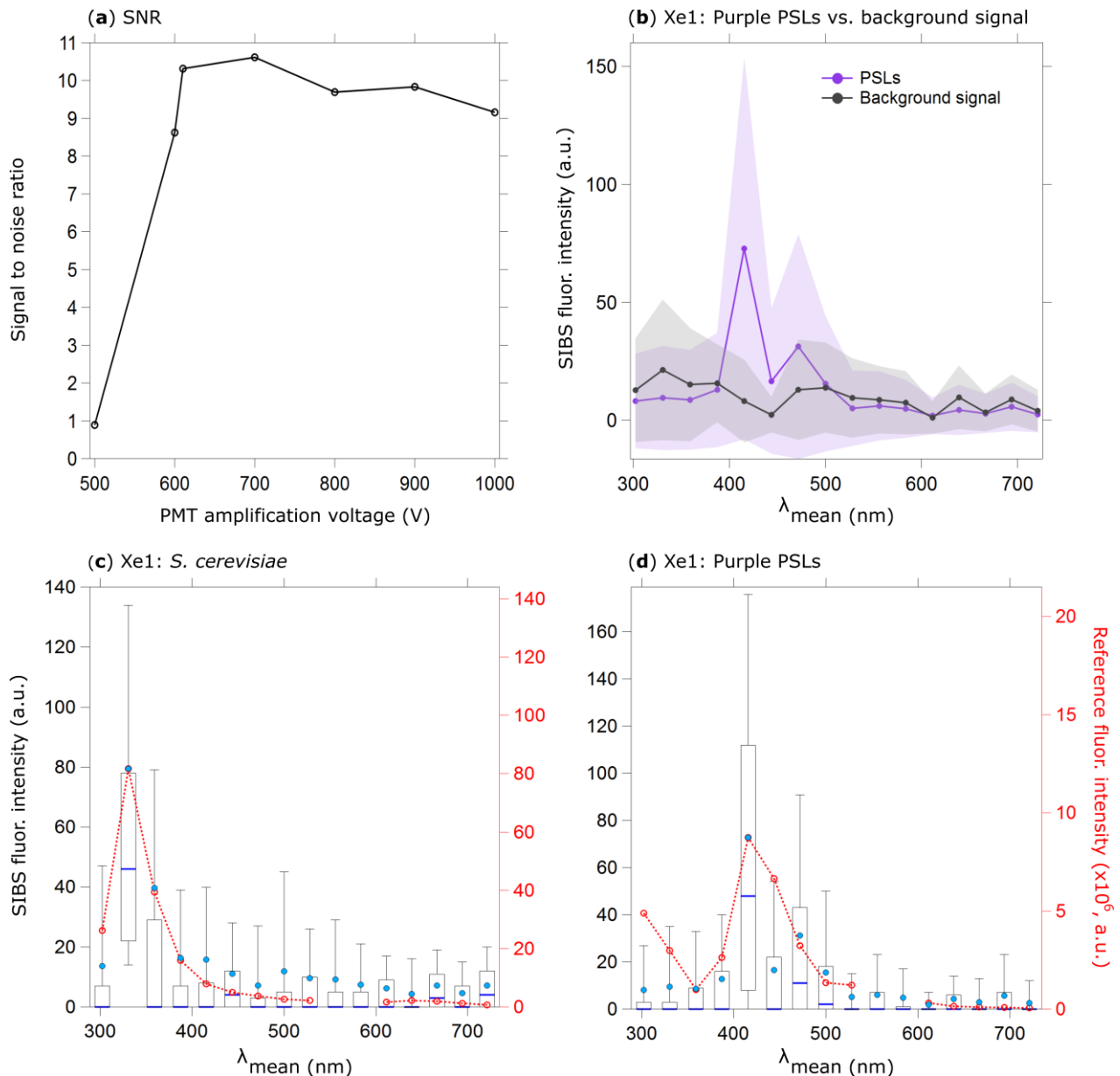
1194 **Figure 3.** Irradiance from xenon flash lamps based on specifications of lamps and optical filters.  
 1195 Purple and blue lines show optical transmission of filters (left axes) applied to select excitation wave-  
 1196 length. Gray bands indicate where filter transmit light relative from the mean wavelength. Red lines  
 1197 show theoretical irradiance values of the xenon flash lamp (right axes): solid line (raw output), dashed  
 1198 line (relative output after filtering). Relative output shown as raw output multiplied by effective ex-  
 1199 citation band of the bandpass filters used in the: (a) SIBS ( $\Delta\lambda_{\text{ex}}(\text{Xenon1}) = \sim 14$  nm;  $\Delta\lambda_{\text{ex}}(\text{Xenon2}) = \sim 36$   
 1200 nm), and (b) WIBS-4A and WIBS-NEO ( $\Delta\lambda_{\text{ex}}(\text{Xenon1}) = \sim 20$  nm;  $\Delta\lambda_{\text{ex}}(\text{Xenon2}) = \sim 36$  nm). Xenon lamp  
 1201 operating conditions: 600 V main voltage, 0.22  $\mu\text{F}$  main capacitance, 126 Hz repetition rate, 500 mm  
 1202 distance. (Data courtesy: Xenon flash lamps / Hamamatsu; Single-band bandpass filters / Semrock).



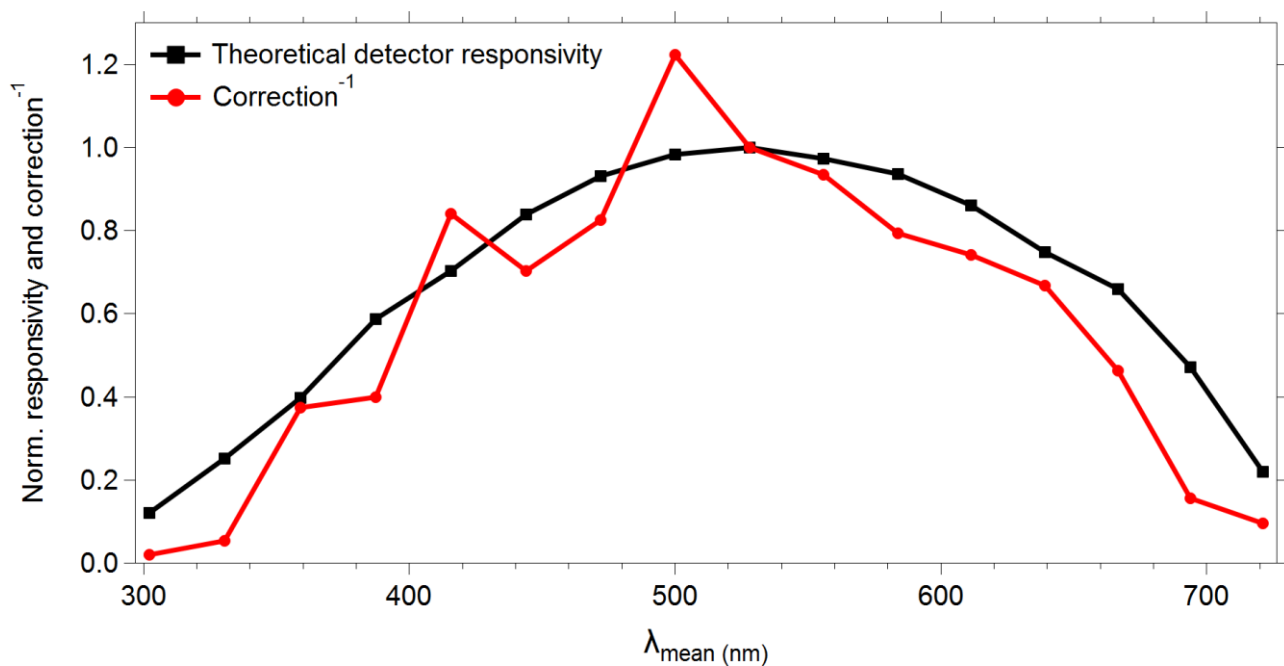
1203  
1204  
1205  
1206  
1207  
1208  
1209  
1210  
1211  
1212  
1213  
1214  
1215



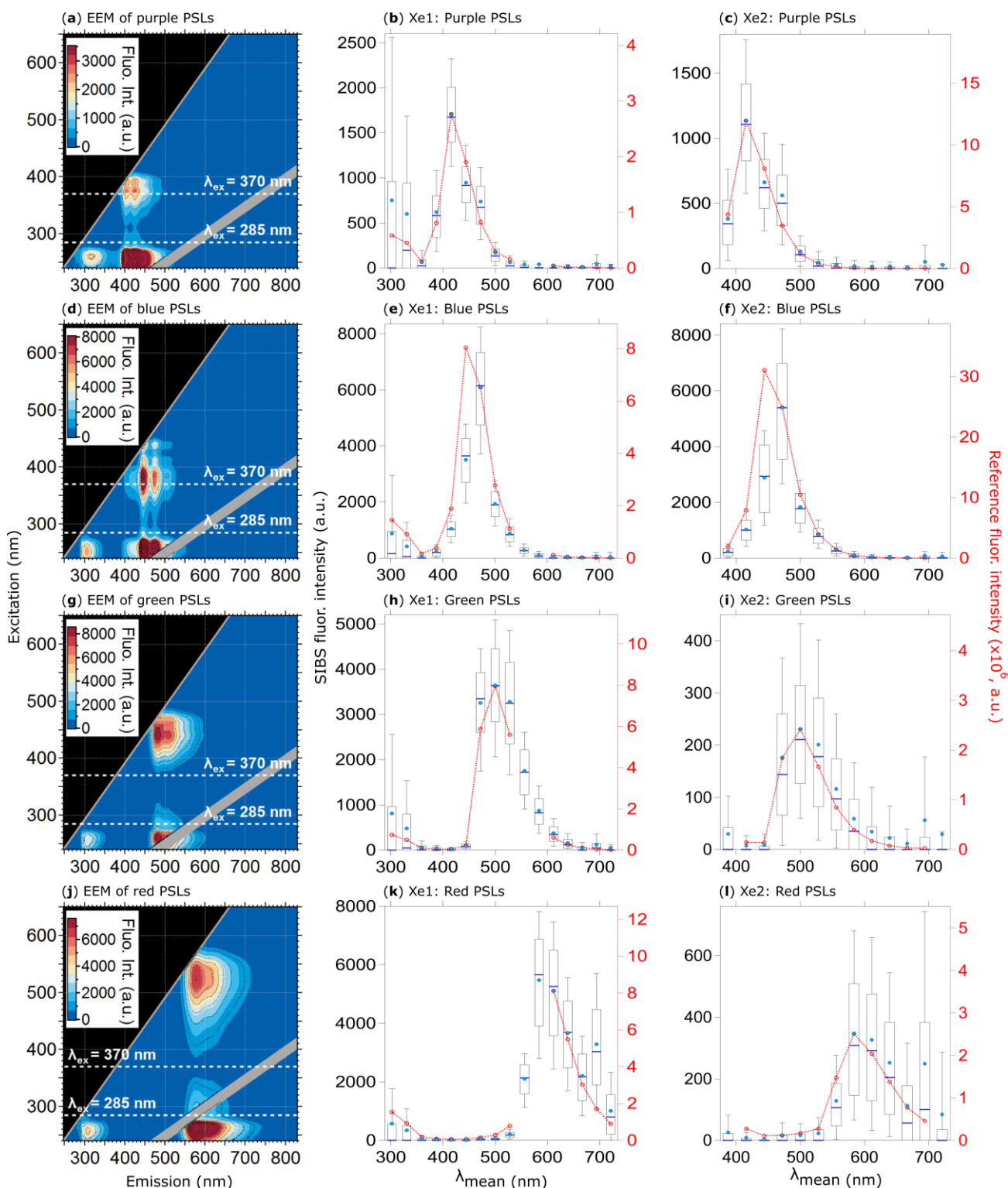
1216 **Figure 4.** Size calibration of SIBS. Black horizontal bars indicate  $1\sigma$  SD as stated by each manufac-  
1217 turer (Table S1). Optical diameter values and related  $1\sigma$  SD are based on a Gaussian fit, which was  
1218 used to average size distributions of several thousand homogeneous particles for each measurement.  
1219 The linear fit (red dashed line) excludes the  $0.356\ \mu\text{m}$  PSL sample (red marker), an outlier potentially  
1220 caused by a poor quality PSL batch. Only non-fluorescent particle standards were used for determin-  
1221 ing the sizing accuracy.



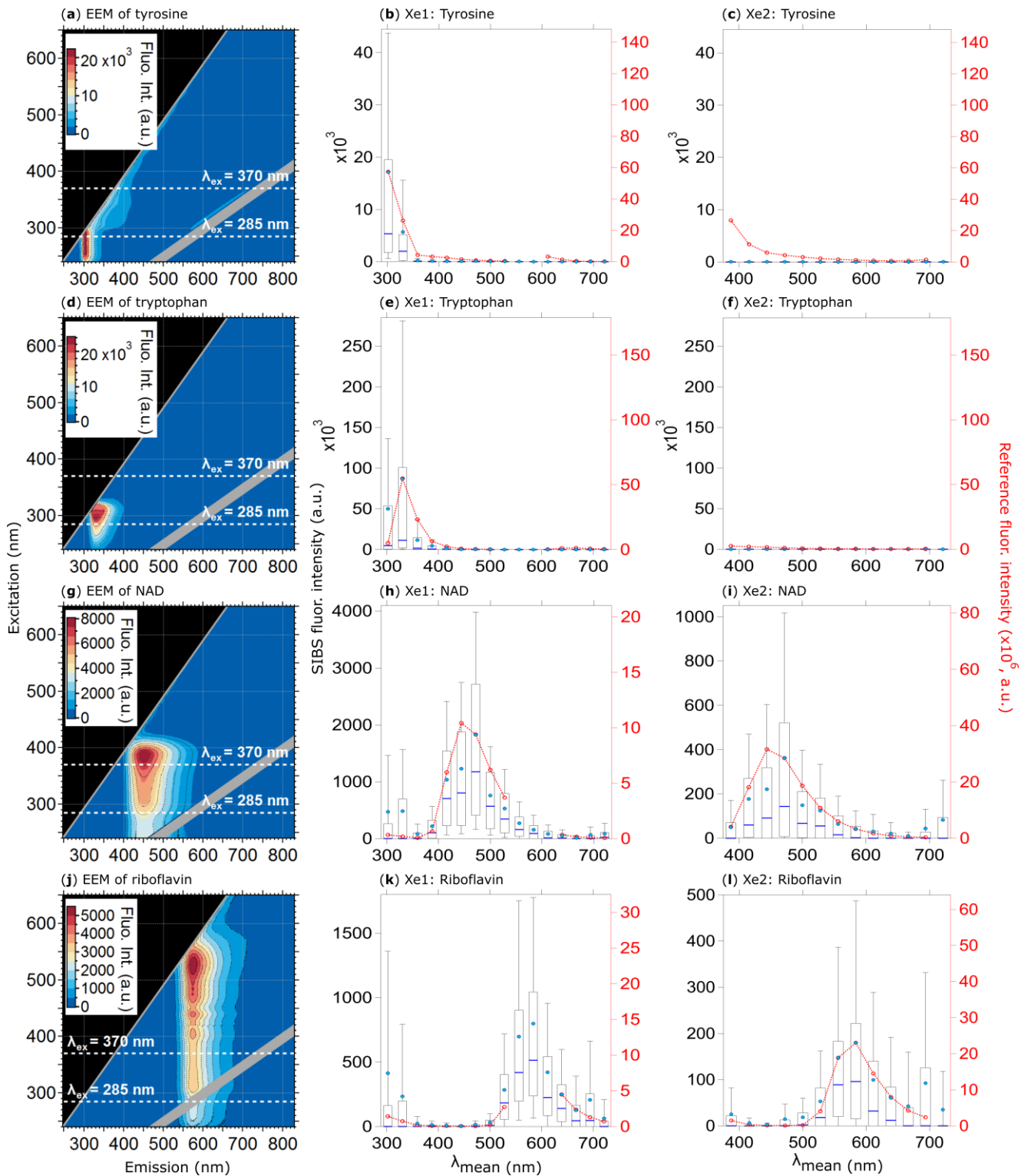
1222 **Figure 5.** SIBS signal to noise ratio (SNR) in (a): emission of 0.53  $\mu\text{m}$  purple PSLs (5260 particles,  
 1223 background signal +  $1\sigma$  SD subtraction) divided by background signal at different PMT amplification  
 1224 voltages (both at Xe1, channel 5, averaged, and uncorrected). Background signal measured over 5  
 1225 min. In (b), fluorescence emission in contrast to background signal at a PMT amplification voltage  
 1226 of 610 V are shown (same parameters as in (a)). Shaded area:  $1\sigma$  SD. Fluorescence intensity values  
 1227 are shown in arbitrary units. Fluorescence emission spectra of (c) *S. cerevisiae* (yeast; 2048 particles,  
 1228 0.5 – 1  $\mu\text{m}$ ) and (d) PSLs (as in (b)). Red dashed lines and markers (right axes) show averaged and  
 1229 re-binned reference spectra. Box and whisker plots (left axes) show SIBS spectra: median (blue line),  
 1230 mean (circle), boxes 75 and 25 percentile, whiskers 90 and 10 percentile. Data coinciding with 1<sup>st</sup> or  
 1231 2<sup>nd</sup> order elastic scattering were removed from reference spectra.



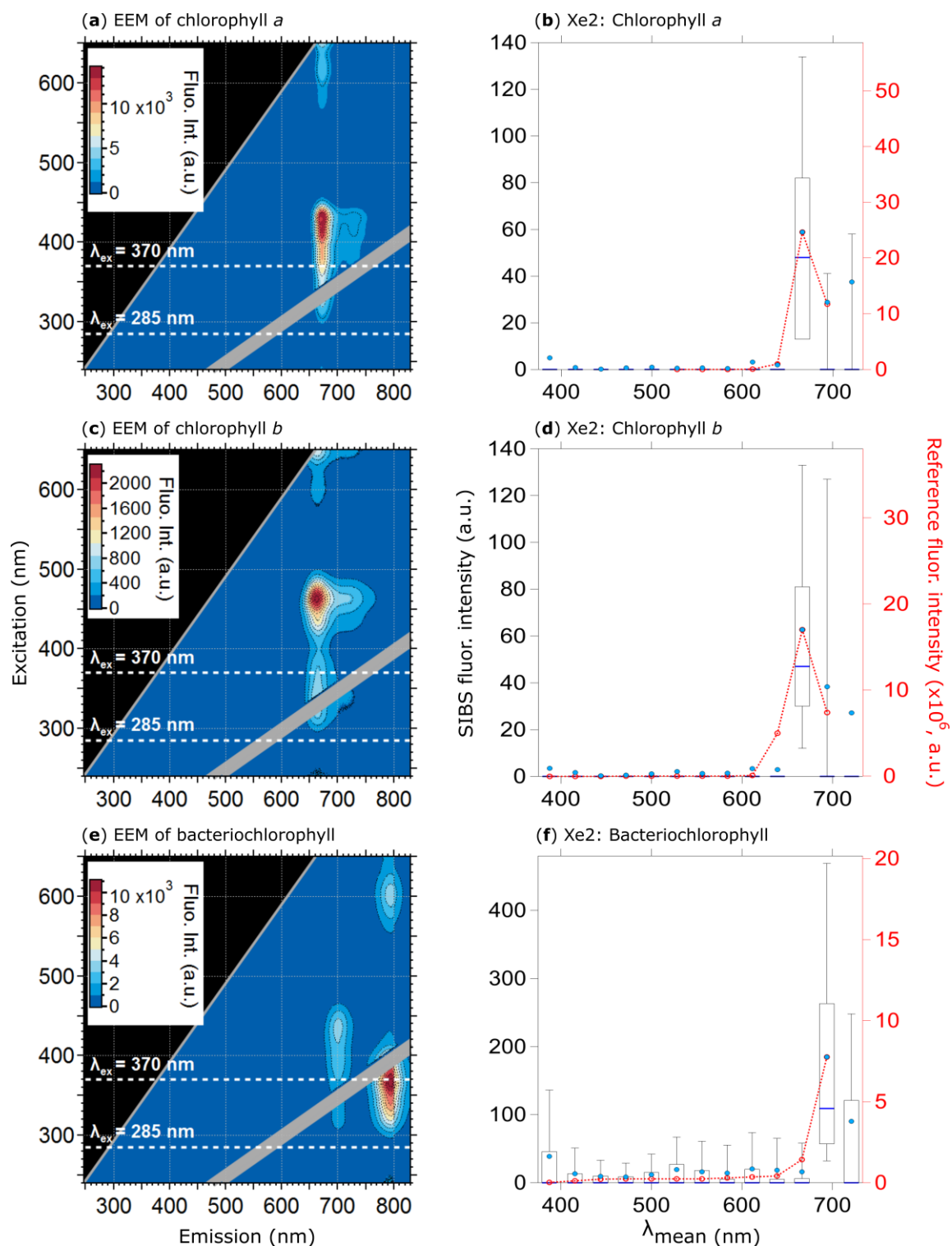
1232 **Figure 6.** Normalized theoretical detector responsivity and spectral correction. Theoretical detector  
 1233 responsivity derived from measured cathode radiant sensitivity multiplied by the diffraction effi-  
 1234 ciency (as shown in Figure S7). Note that red line shows inverse of spectral correction to match  
 1235 detector response.



1236 **Figure 7.** Fluorescence emission spectra of PSLs. Steady-state fluorescence signatures displayed as  
 1237 EEMs (left column) and spectra at Xe1 and Xe2 (middle, right columns) for: 2.07  $\mu\text{m}$  purple (**a**, **b**  
 1238 and **c**, 1082 particles), 2.1  $\mu\text{m}$  blue (**d**, **e** and **f**, 1557 particles), 2  $\mu\text{m}$  green (**g**, **h**, and **i**, 1174 particles),  
 1239 and 2  $\mu\text{m}$  red PSLs (**j**, **k**, and **l**, 1474 particles). Within EEMs: white dashed lines show SIBS excitation  
 1240 wavelengths ( $\lambda_{\text{ex}} = 285$  and  $370$  nm), grey diagonal lines indicate 1<sup>st</sup> and 2<sup>nd</sup> order elastic scatter-  
 1241 ing bands (both bands were subtracted automatically by the Aqualog V3.6 software). Red dashed  
 1242 lines and markers (right axes; middle, right columns): averaged and re-binned reference spectra.

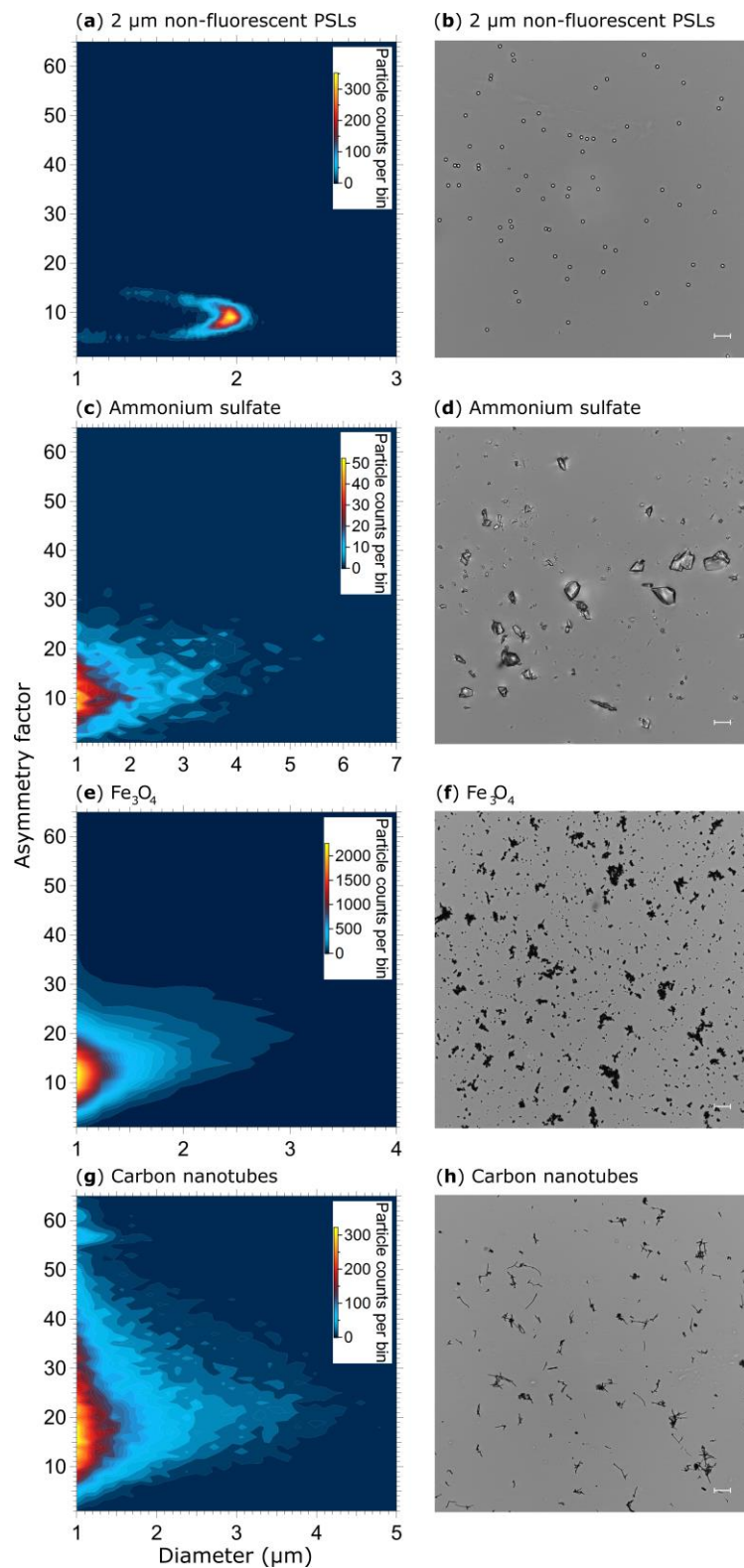


1243 **Figure 8.** Fluorescence emission spectra of biofluorophores. EEMs (left column) and spectra at Xe1  
 1244 and Xe2 wavelengths (middle and right columns) shown for: tyrosine (a, b, and c, 209 particles),  
 1245 tryptophan (d, e, and f, 193 particles), NAD (g, h, and i, 376 particles), and riboflavin (j, k, and l,  
 1246 205 particles). Red dashed lines and markers (right axes; middle, right columns): averaged and re-  
 1247 binned reference spectra. All biofluorophores were size-selected between 1 and 2  $\mu\text{m}$ .

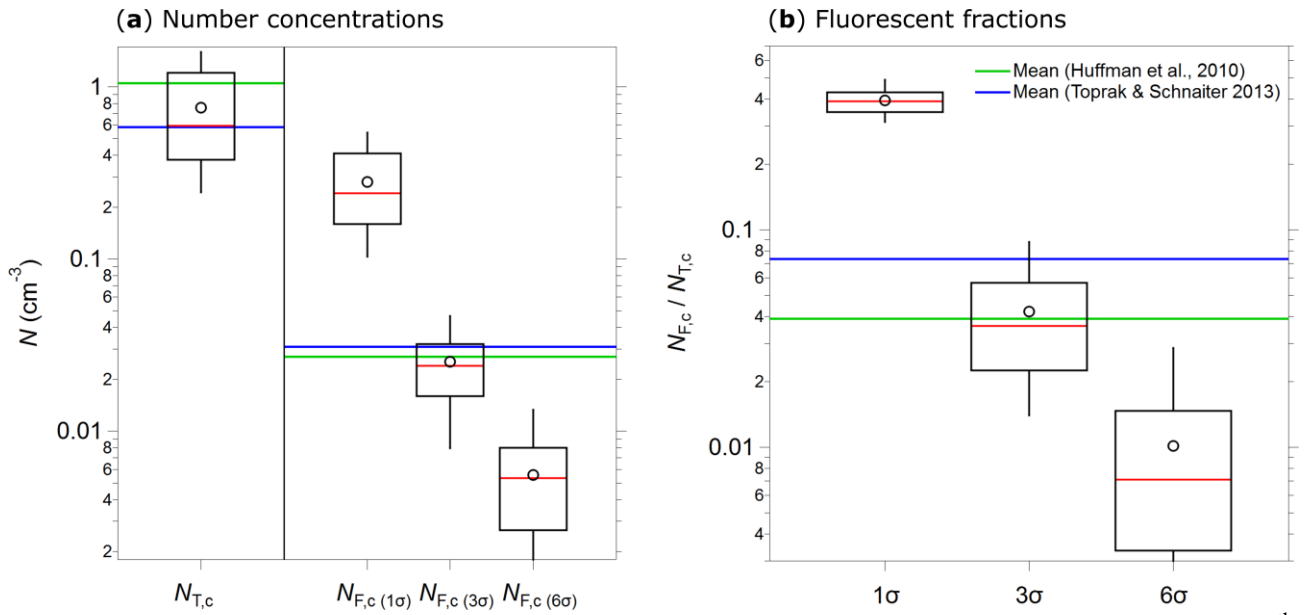


1248 **Figure 9.** Fluorescence emission spectra of three chlorophyll types. Highlighted are EEMs (left col-  
 1249 umn) and spectra at Xe2 (right columns) for: chlorophyll *a* (**a** and **b**, 370 particles), chlorophyll *b* (**c**  
 1250 and **d**, 585 particles), and bacteriochlorophyll (**e** and **f**, 633 particles). Red dashed lines and markers  
 1251 (right axes; right column): averaged and re-binned reference spectra. Size range chlorophyll *a* and *b*:  
 1252 0.5 - 2  $\mu\text{m}$ , size range bacteriochlorophyll: 0.5 - 1  $\mu\text{m}$ . Emission spectra at Xe1 are excluded due to  
 1253 a fluorescence artifact caused by solved components from the polymer of the aerosolization bottles  
 1254 (Fig. S11).

1255  
1256  
1257  
1258  
1259  
1260  
1261  
1262  
1263  
1264  
1265  
1266  
1267  
1268  
1269  
1270  
1271  
1272  
1273  
1274  
1275  
1276  
1277  
1278  
1279  
1280  
1281  
1282  
1283



1284 **Figure 10.** Particle asymmetry. Shown are particle density histograms (left column) and microscopy  
1285 images (right column) for: 2  $\mu\text{m}$  non-fluorescent PSLs (**a** and **b**, 17836 particles), ammonium sulfate  
1286 (**c** and **d**, 3496 particles),  $\text{Fe}_3\text{O}_4$  (**e** and **f**, 65097 particles), and carbon nanotubes (56949 particles, **g**).  
1287 Scale bar (right column) indicates a length of 10  $\mu\text{m}$ .



1288 **Figure 11.** Integrated coarse particle (1-20  $\mu\text{m}$ ) number concentrations, measured between the 12<sup>th</sup>  
 1289 and 18<sup>th</sup> of April 2018 (5 min average), for total particles ( $N_{T,c}$ , fluorescent and non-fluorescent) and  
 1290 coarse fluorescent particles ( $N_{F,c}$ ) after 1, 3, and 6 $\sigma$  SD background signal subtraction (a). The fluo-  
 1291 rescent fractions of integrated coarse particle number concentrations ( $N_{F,c} / N_{T,c}$ ) at 1, 3, and 6 $\sigma$  SD  
 1292 are shown in (b). Median (red line), mean (black circles), boxes 75 and 25 percentile, whiskers 95  
 1293 and 5 percentile (a and b). Data from Huffman et al. (2010) (green lines) and Toprak & Schnaiter,  
 1294 (2013) (blue lines) were taken for comparison (a and b).